Taylor & Francis
Taylor & Francis Group

REVIEW ARTICLE

🔓 OPEN ACCESS   Check for updates

Nonlinear optics on nano/micro-hierarchical structures on metals: focus on symmetric and plasmonic effects

Yoichi Ogata and Chunlei Guo

The Institute of Optics, University of Rochester, Rochester, NY, USA

ABSTRACT

In this review, the authors study their creation of nano/micro-hierarchical structures on Ag and Ni substrates by femtosecond laser treatment and their investigation of their optical second-harmonic generation (SHG) signal intensities by SHG spectroscopy. The authors obtained the nanostructure-covered microgroove and microcube structures. These hierarchical surface structures were found to modify significantly the optical nonlinearity of the metal surfaces. The macroscopic symmetry of the surface's shapes influenced SHG, and the excitation of surface plasmons enhanced SHG. On the other hand, the nanostructures on the microstructures had an additional effect on the generated SHG. For the microcube structures, the additional SHG emission was suppressed by removing a large amount of nanostructures. Left SHG was discussed by the effect of the propagating delay.

1. Introduction

Nonlinear optical phenomena in nanostructured materials have been challenging our perceptions of nonlinear optical processes that have been explored since the invention of lasers [1]. The symmetry parameter is important because the symmetry of nanostructures should have an influence on their dielectric property through the electric wave function in their constituent atoms and bondings. In particular, second-order nonlinear optical phenomena are forbidden for centrosymmetric structured materials [2,3]. Hence, the second-order nonlinear optical process should be sensitive to the symmetry of nanostructured shape [4].

Optical second-harmonic generation (SHG) is a coherent nonlinear optical process and its efficiency depends not only upon the electronic properties but also upon the symmetry of the geometrical structure of the medium [2,5,6]. In general, SHG does not generate in centrosymmetric bulk media [2]. Recently, advances of nanofabrication techniques [7,8] have enabled control of the sizes, shapes, and alignment of nanostructures of a wide range of materials, and their SHG responses have been investigated. For example, the reports for SHG responses from the GaAs nanoneedles grown by the chemical vapor deposition method [9], the nanocups deposited Au by electron-beam evaporation on to silica nanoparticles [10], the ZnO nanorods grown on glass substrates by means of the low-temperature chemical bath method [11], the Pt nanowires created by the physical

vapor deposition method [12], and the Au nanoholes fabricated by the focused ion beam method [13] attracted most researchers. These SHG processes are used in a wide range of applications, such as developing devices for optical processing [14], nonlinear imaging [4], and phase-sensitive amplification [15]. Because nonlinear processes through photon–photon interactions are intrinsically weak, studies on enhancement of nonlinear efficiency are crucial [16].

So far, enhancement of SHG responses by surface plasmons (SPs) has been studied extensively [17–19]. Surface plasmons are coherent electron oscillations localized on a metal surface [18,20]. Because SHG light intensity is proportional to the incident light intensity squared, the SP-induced electric field enhancement at the surface yields significantly enhanced SHG emission. As representative works, Quail and Simon [21] and Pipino et al. [22] have focused on studying SHG enhanced by propagating SPs on metal nanograting. They found that the diffracted SHG was enhanced at a specific incident angle. Also, Baida et al. [23] and Hubert et al. [24] have focused on studying SHG enhanced by localized SPs on metal nanostructures. They found that the SHG was enhanced at a specific incident wavelength. However, the good development of nonlinear optical devices requires detailed understanding and modeling of the nonlinear optical response of nanoscale metallic systems.

Recently, the femtosecond (fs) laser has been shown to be an effective tool for producing surface structures on the nanoscale and microscale [25,26]. For example, a number of nano/micro-hierarchical

CONTACT Yoichi Ogata ✉ ogachi.yo@gmail.com; Chunlei Guo ✉ chunlei.guo@rochester.edu
*Present address: Center for Advanced Photonics, RIKEN 519-1311 Aoba, Sendai, Japan, 980-0845, Japan

patterns were created by fs laser surface structuring, such as nanostructure-covered laser-induced periodic surface structures (NC-LIPSSs) [26]. The uniqueness of the configuration is that they contain a hierarchy of nanostructures superimposed on microstructures. Two layers of these hierarchical patterns are seen; random nanostructures at tens to hundreds of nanometers are superimposed on microscale periodic grooves. The periodicity of microgrooves for NC-LIPSSs is on the order of the generating laser wavelength (~800 nm).

So far, we have produced NC-LIPSSs on many kinds of metal surfaces. We found that NC-LIPSSs could significantly change the optical properties of the metal surfaces [26,27]. Both microscale periodic grooves and nanostructures on NC-LIPSSs can affect SPs; the grooves can couple optical pulse energy to propagating SPs, while the nanostructure can couple incident photons to localized SPs. Therefore, NC-LIPSSs are likely to exhibit unusual SP-induced nonlinear optical effects, and this can be seen from one of our recent studies on photoelectron emission from NC-LIPSSs on Pt [27]. Essentially, nanostructures on LIPSSs change the dispersion relation of the SP modes [28]. With the excitation of SPs, we observed multiphoton nonlinear photoelectron emission from the NC-LIPSSs. Following this work, we set out to study the nonlinear optical effects of the metallic NC-LIPSSs.

Despite the extensive research on the SP-assisted nonlinear processes in pure metals, hybrid, or composite materials [22,29–33], a systematic study on the effects of micro/nano-hierarchical structures on nonlinear optical processes is currently lacking. As mentioned above, both nanostructures and microstructures are important for generating SPs. Accordingly, a systematic study of the combined effect of nano/micro-hierarchical structures is necessary for its potential applications of hierarchical structures in future nonlinear optical devices. The nanostructure-covered micro cubes (NC-MCs) is a novel hierarchical surface structure which consists of micro cubes covered by a large number of nanostructures. Throughout this study, we shall relate to both NC-LIPSSs and NC-MCs. One interesting aspect of the structure is that SPs are excited by the dominant features of the different scales of the surface structures. The major difference between the two types of structure is that different types of SP are excited by the dominant features on the different types of surface structure. For example, the microgrooves on NC-LIPSSs favor the excitation of propagating SPs (Figure 1(a)). However, the smaller structures on each type of hierarchical structure can excite additional SPs: nanostructures on NC-LIPSSs can generate localized SPs (Figure 1(b)). The microcubes on the NC-MCs induce lightning rod effect (LR) (Figure 1(c)); however, the smaller structures on the hierarchical structure can excite additional SPs: nanostructures on NC-MCs can generate localized SPs (Figure 1(b)). By performing a systematic investigation of SPs induced by different individual structures, the interactions of SPs induced by different individual structures, and the final combined SPs (such as PSP/LSP or LR/LSP as illustrated in Figure 1(d) and 1(e)) due to the hierarchical structures, we expect that we can control the SHG efficiency in nano/microstructures. In this work, we create the NC-LIPSSs and NC-MCs on Ag and Ni through laser ablation methods and investigate their SHG responses from the viewpoint of 'symmetry' and 'SP' [34,35]. By comparing the signals from NC-LIPSSs and NC-MCs with the signal from nanostructures and microstructures, we characterize the relation between nanostructures and/or microstructures and SHG.

2. Materials and methods

Our experimental setup employed two amplified Ti: Sapphire fs laser systems, a high-energy system, and a high-repetition-rate system. The high-energy fs laser system generated 60-fs pulses with a central wavelength of 800 nm; the average power of the laser was 1.2 W at 1 kHz repetition rate. The high-repetition-rate laser system generated 65-fs pulses at a central wavelength of 810 nm; the average power of the laser was 400 mW at 273 kHz repetition rate.

2.1. Laser treatment of the Ag surface

As described in [26], we first produced a Ag sample covered with NC-LIPSSs using the high-energy fs laser system. An experimental setup for surface nano/microstructuring on Ag is shown in Figure 2(a). The laser polarization was oriented to the ground using a polarizer, and a neutral density (ND) filter was used to adjust the laser power irradiated on the sample. The laser fluence was set at ~0.150 J/cm^2. Then, by focusing the beam on to a Ag sample mounted on a stage, we obtained the Ag NC-LIPSS sample.

2.2. Laser treatment of the Ni surface

We next produced a Ni sample covered with NC-MCs. We established a new setup using the high-energy fs laser system, as provided in a previous study [36]. An experimental setup for surface nano/microstructuring on Ni is shown in Figure 2(b). The laser beam from the light source was divided into two beams by using a beam splitter. In an optical path, a half-wave plate (HWP) was used to rotate the laser polarization by 90°, and a ND filter was used to adjust the laser power irradiated on the sample. The laser fluence was set to 0.137 J/cm^2. The two beams were controlled using a chopper. The number of pulses per pulse burst was determined to be one. If the chopper frequency is set at 500 Hz, the time interval when the chopper slot is open for a specific beam is 0.001 s; therefore, the two beams alternately passed through
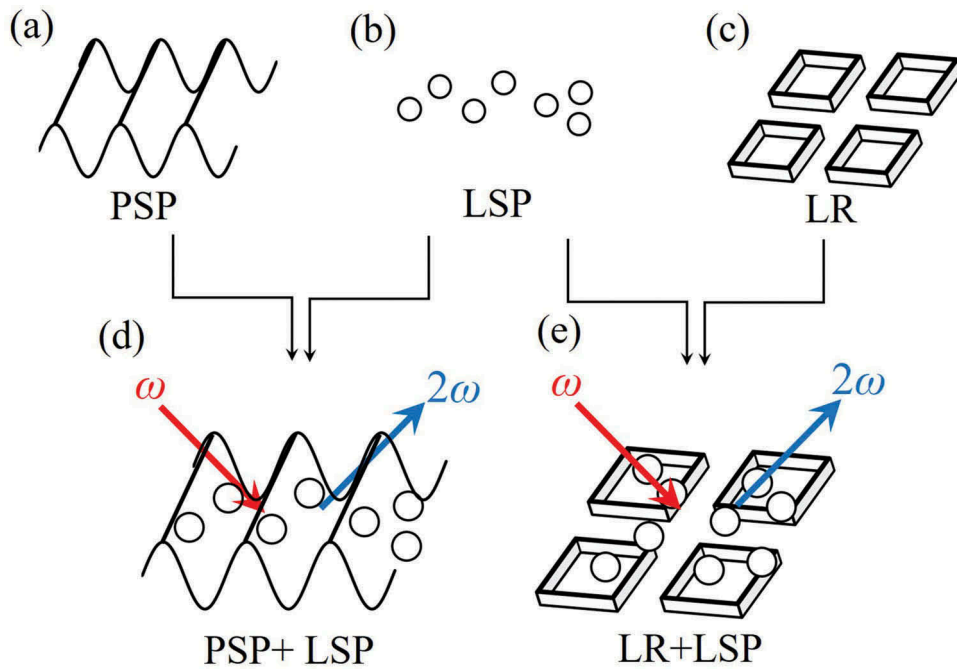
Figure 1. (a–c): Image of individual structures for (a) microgroove, (b) nanostructures, and (c) microcube. (d, e): Image of SHG spectroscopy on combined structures for (d) NC-LIPSS and (e) NC-MC. PSP: propagating surface plasmon, LSP: localized surface plasmon, LR: lightning rod.
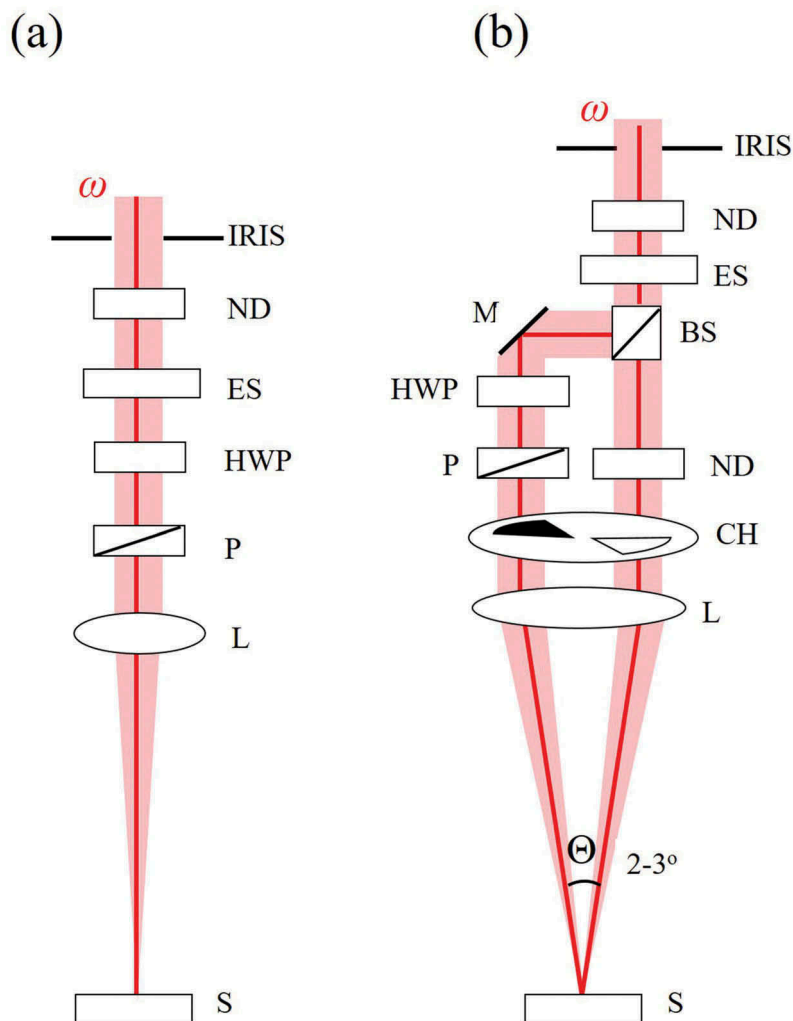

Figure 2. Experimental setup for surface nano/microstructuring on (a) Ag and (b) Ni. CH: chopper; HWP: half-wave plate; P: polarizer, ND: neutral density filter; L: lens; S: sample; ES: electric shutter; M: mirror; BS: beam splitter. Θ is defined as the angle between two beams.

the chopper pulse by pulse. Then, by focusing the beams on to a Ni sample mounted on the stage, we succeeded in fabricating the Ni NC-MC sample.

Figure 3(a,b) shows the optical configuration for the sample preparation. Using this method, two-dimensional arrays of the NC-LIPSS and NC-MC sample were fabricated, and part of them was observed by an optical microscope, as seen in Figure 3(c,d). After these laser treatments, the surface morphologies of NC-LIPSSs and NC-MCs were characterized by using a scanning electron microscope (SEM). Figure 3(e,f) shows the SEM image of the laser-treated micro/nano-hierarchical structures on Ag and Ni, respectively. Figure 3(g,h) shows that microgrooves and microcubes are covered with nanostructures. The average measured periods Λs of the microgrooves and microcubes on Ag and Ni were 672 and 600 nm, respectively. The measured depth h of both microstructures was ~100 nm.

Before the SHG measurements of the Ag sample, the hierarchical structures were coated with a thin SiO layer (5.3 nm thick) by physical vapor deposition in a UHV chamber. The protective SiO layer serves two purposes: (1) to protect the surface from atmospheric gases, especially oxidation; and (2) to avoid any damage to the surface [5]. This coating did not affect the conclusions drawn from our study because the SiO layer was very thin and thus was transparent to both 800 and 400 nm wavelength light on a metal–SiO interface.
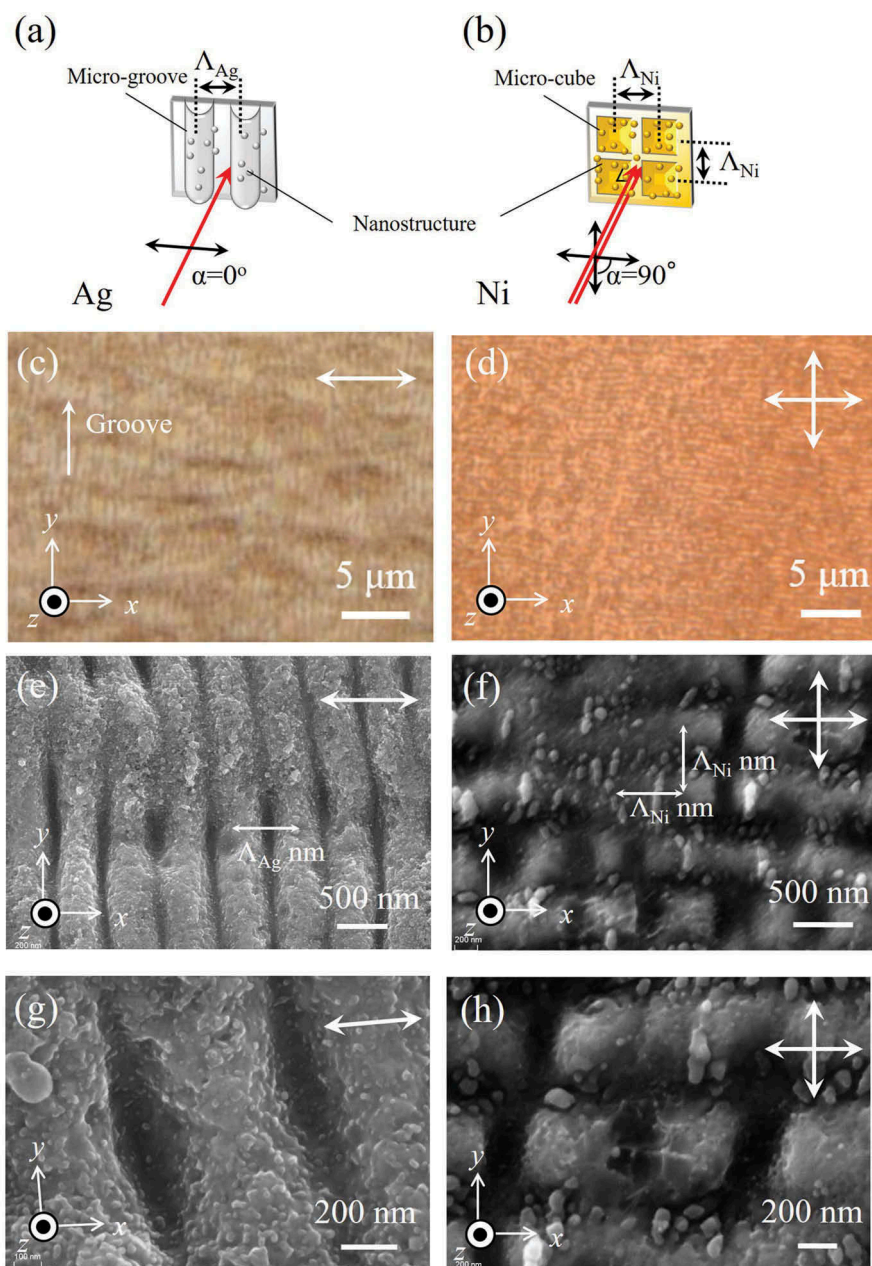
Figure 3. Optical configuration for surface nano/microstructuring on (a) Ag and (b) Ni. The laser polarization is indicated with a double arrow in these plots. α is the angle between the two laser polarization directions. Optical microscope image of (c) Ag and (d) Ni samples. SEM images of NC-LIPSSs on Ag showing (e) microgrooves and (f) microcubes. (g, h): Zoomed views, showing smaller features of (e) and (f).

2.3. SHG measurement for the Ag and Ni samples

Once the sample was fabricated using a high-energy fs laser system, the SHG measurements of the Ag and Ni samples were performed using the high-repetition and high-energy laser system, respectively. Figure 4 shows the configuration of the SHG intensity measurements of the Ag and Ni samples. The p- and s-polarized light at ~800 nm were passed through an orange filter to cut the SHG photons from optics and were focused on to the Ag NC-LIPSS and Ni NC-MC samples at an incidence angle of 45° through a lens. The laser fluences were set at ~25.5 and ~30.9 mJ/cm² respectively. Here, the direction for p-polarization corresponds to the inner production between the x- and z-directions. The direction for s-polarization corresponds to the y-direction. The rotation angle φ was defined as the angle between the incident plane and the groove direction. When φ is set at 0°, the incident light travels in the x-direction, as shown in Figure 2(a). In the experiment with the Ag sample, we studied the dependence of SHG on the incident beam angle and the laser polarization. For this, the sample was mounted on two rotation stages. In the experiment with the Ni sample, we studied the dependence of SHG on the laser polarization. For this, the sample was mounted on just one rotation stage. The generated SHG reflection was passed through a blue filter (BG39) and a band-pass filter (FB400-10) to filter the fundamental frequency, and, subsequently, a polarizer was used to select the p- and s-polarization for Ag and Ni samples, respectively. To account for the hyper-Rayleigh scattering (HRS) [37,38], the reflected SHG light was collected through a focusing lens with a large numerical aperture. Here, HRS is incoherent second-harmonic (SH) scattering from small feature structures based on Mie theory; up to now, HRS signals from spherical and non-spherical lacking centrosymmetric structures have been observed [39,40]. Hence, the consideration of HRS is important, and the experimental setup has been referred to in some papers [38,41]. Following polarization selection, the reflected SHG light signals were detected by a photomultiplier tube (PMT). In order to get high signal-to-noise ratio of the SHG intensity, the SHG light intensity pulse was accumulated for ~7 min for each SHG data point.

3. Results and discussion

3.1. SHG signal from Ag samples

We first defined the relationship between the reflected SHG light $I(2\omega)$ and the nonlinear susceptibility $\chi^{(2)}$ of the metallic groove sample, as done in a previous study [17]. The p-polarized SHG intensity $|E_p(2\omega)|^2$ {= $I_p(2\omega)$} generated using the $\chi^{(2)}_{XXZ}$ element is given as:

$$|E_p^R(2\omega)|^2 \propto |L_X(2\omega)\chi^{(2)}_{XXZ}E_{X,\mathrm{loc}}E_{Z,\mathrm{loc}}(\omega)|^2 \qquad (1)$$

χ_{ijk} is the nonlinear susceptibility, with i, j, and k representing x-, y-, and z-directions. The coordinate system is oriented so that the X and Y coordinates are in the plane and the Z coordinate is in the direction normal to the substrate surface. $L(2\omega)$ and $L(\omega)$ represent the local field factors at the SHG and fundamental frequency containing the contribution by the plasmonic excitation. The local electric field E_{loc} has the relation $E_{\mathrm{loc}} = L(\omega)E(\omega)$. Consequently, Equation (1) shows that
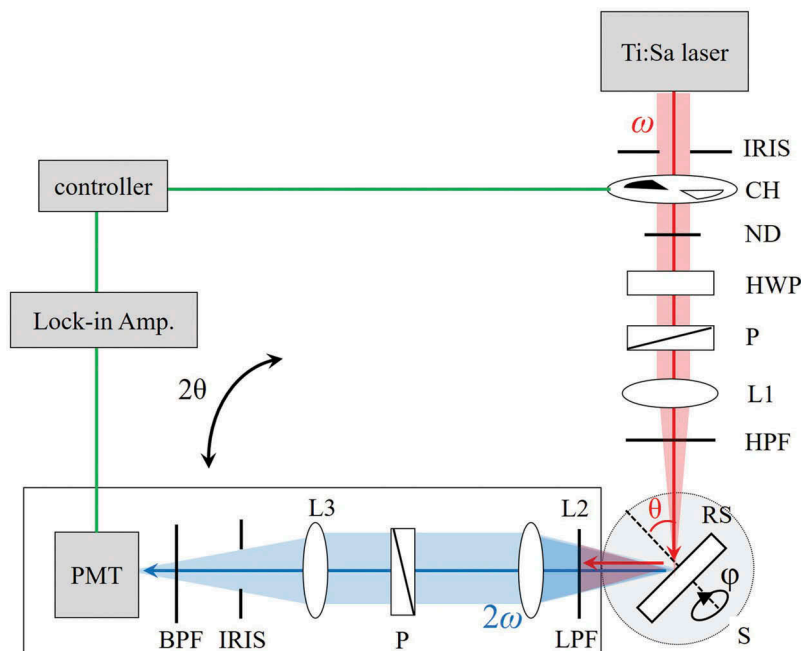
Figure 4. Experimental setup of SHG measurements. CH: chopper; HWP: half-wave plate; P: polarizer; ND: neutral density filter; L: lens; RS: rotation stage; S: sample, HPF: high-pass filter; LPF: low-pass filter; BPF: band-pass filter; PMT: photomultiplier tube.

the s-polarized SHG intensity $|E_p(2\omega)|^2$ depends on the local electric field E_{loc} of the X- and Z-direction component.

3.1.1. Power dependence of the SHG from Ag NC-LIPSSs

Figure 5 shows the excitation power dependence of the SHG signals measured on Ag NC-LIPSSs. The data show that the SHG signal has a nearly quadratic dependence on the excitation intensity (slope: 1.81), which indicates a characteristic of the second-order nonlinear processes. The conversion efficiency from fundamental to SHG light photons for the Ag sample was ~10^{-12} at maxima for p-in/p-out polarization configuration.

3.1.2. Incident angle dependence of the SHG from Ag NC-LIPSSs

We next measured the SHG intensity from a Ag sample as a function of the incident angle θ. Figure 6 shows the angle-resolved SHG intensity from the Ag NC-LIPSSs in p-in/p-out polarization configuration. When the laser polarization was parallel to the microgrooves (the E//groove configuration), the SHG intensity did not vary noticeably with the incident angle θ. However, when the laser polarization was normal to the microgrooves (the E⊥groove configuration), SPs could be excited using the laser beam, and the SHG signal was significantly enhanced between $\theta = 40°$ and 55°. We believe that this is owing to the enhancement of electric field E by SP excitation in the propagating mode. At an incident angle of 45°, the SHG intensity for the E⊥groove configuration was ~fourfold stronger than that for the E//groove configuration. We also observed that the NC-LIPSSs on the Ag relax the phase-matching conditions for SP excitation owing to the mismatch of groove period Λ or broadened wave vector **k** on NC-LIPSSs [27] and significantly broaden the range of angular-coupling, leading to an enhanced SHG light emission over a broad range of incident angles. We also observed SHG for
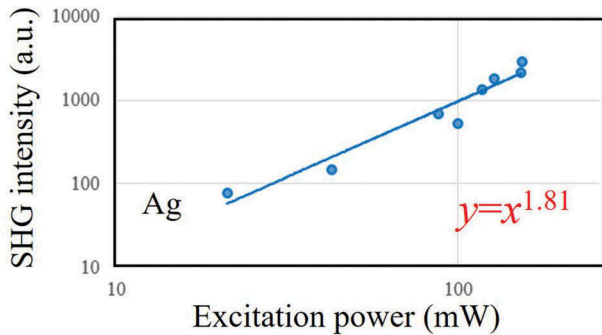
Figure 5. Excitation power dependence of the observed SHG intensity for the Ag NC-LIPSSs plotted on a log–log scale. The slope value for the fits to these data is ~2, confirming the second-order nature of the emitting light.
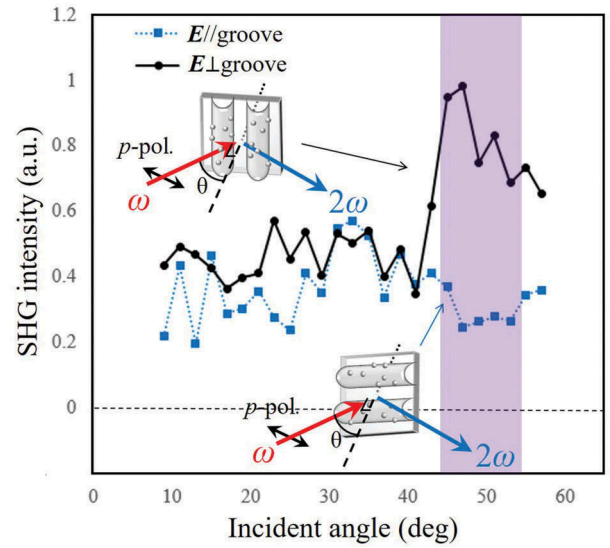
Figure 6. (a) The SHG intensities from the Ag NC-LIPSSs as a function of the incident beam angle with polarizations either parallel or normal to the grooves. The data points are connected by lines to guide the eye. The color part from 45° to 55° shows broadened SP resonance.

other incident angles. We believe this is due to the nanostructures covering the microstructures. From these data, we say that the SHG from nanostructures does not dominate at incident angles.

3.1.3. Sample rotation angle dependence of the SHG from Ag NC-LIPSSs

To investigate the origin of the anisotropic enhancement of the generated SHG, we analyzed the nonlinear optical susceptibility $\chi^{(2)}$ of the NC-LIPSS surface of Ag. As indicated in Appendix 1, because the shape of Ag microgrooves had (quasi-)C_{2v} symmetry, five independent nonlinear susceptibility elements, $\chi^{(2)}_{XXZ}$, $\chi^{(2)}_{ZXX}$, $\chi^{(2)}_{ZZZ}$, $\chi^{(2)}_{YYZ}$, and $\chi^{(2)}_{ZYY}$, are permitted [2,6]. Here, the subscripts X, Y, and Z indicate the laboratory coordinates. Symmetry breaking in the Z-direction does not exist, which disobeys the fact that there is a symmetry breaking in the Z-direction when the non-zero nonlinear susceptibility element has an odd number of Z in the suffixes. From this, the contribution of $\chi^{(2)}_{ZZZ}$ should be zero. In addition, symmetry breaking in the Y-direction does not exist. From this, the contributions of $\chi^{(2)}_{XXZ}$ and $\chi^{(2)}_{ZXX}$ are much stronger than the contributions of $\chi^{(2)}_{YYZ}$ and $\chi^{(2)}_{ZYY}$. We also studied an s-in/p-out polarization configuration, and we did not find any SHG in this configuration (not shown here). This allowed us to rule out $\chi^{(2)}_{ZXX}$; thus, the contribution is determined by $\chi^{(2)}_{XXZ}$. It should lead to a pattern with two lobes at $\varphi = 0°$ and 180° in p-in/p-out polarization. From the above, we estimate that the $\chi^{(2)}_{XXZ}$ forming a $\cos(\varphi)$ function strongly dominates on the SHG intensity from the NC-LIPSSs on Ag. Thus, the $|\chi^{(2)}|^2$ curve was fitted by a $\cos^2(\varphi)$ function.

NC-LIPSSs in this study were created using a normal incident beam. In this case, the periodicity Λ of the

surface grating formed by interference between the incident laser light and the excited SP wave is given by

$$\Lambda = \lambda \left(\frac{\varepsilon' + \varepsilon_d}{\varepsilon' \varepsilon_d} \right)^{\frac{1}{2}} \qquad (2)$$

with the grooves formed normal to the electric field direction [26,27,42]. Here, λ is the incident light wavelength, and ε' and ε_d are the dielectric constants of the real part and of the surrounding dielectric material, respectively. When the laser ablation is performed in air, $\varepsilon_d = 1$. For the smooth Ag sample, periodicity of the grooves Λ was calculated as $\varepsilon_1 = -29.7$ at $\lambda = 800$ nm for the Ag [43]. By using Equation (2), Λ was found to be 786 nm for the Ag sample. However, the observed periodicity was about 672 nm for the Ag sample (Figure3(e,g)). By using the observed periodicity value, we found that $\varepsilon'_{Ag} = 2.4$ for the Ag sample. We believe that this effective dielectric constant arises from the nanostructures on top of the microstructures. Using the effective dielectric constant, we next investigated the electric field distribution at $\theta = 45°$ on a periodic groove surface on the Ag sample.

As mentioned above, the local enhancement of an electric field by metallic nanostructures can enhance the SHG response [13]. We should notice that the SP enhancement of SHG is very sensitive to the linear dielectric $\varepsilon^{(1)}$, leading to the enhancement of the incident electric field E to fourth order, as explained in Appendix 2. To find the origin of the SP-enhanced SHG, we calculated the local electric field E_{loc} intensity on the NC-LIPSSs by using the finite difference time domain (FDTD) method. Here we used commercial software (Lumerical Solutions, Canada, https://www.lumerical.com/tcad-products/fdtd/). The electric field distribution for the x-direction at $\theta = 45°$ is shown in Figure 7(b). Here, the red and blue color scales in Figure 7(b) indicate the distributions of positive and negative change, respectively, for electric field E. A propagating surface wave on a continuous metal–dielectric interface is a SP polariton. SP polaritons were clearly observed, implying propagating surface waves on the continuous metal–dielectric interface. The value in Figure 7(b) indicates the maximal electric field magnitude $|E|_{max}$ calculated in the simulations. At $\varphi = 0°$ and 180° ($E{\perp}$groove), the values of $|E|_{max}$ were higher, and at $\varphi = 90°$ and 270° (E//groove), the $|E|_{max}$ value was
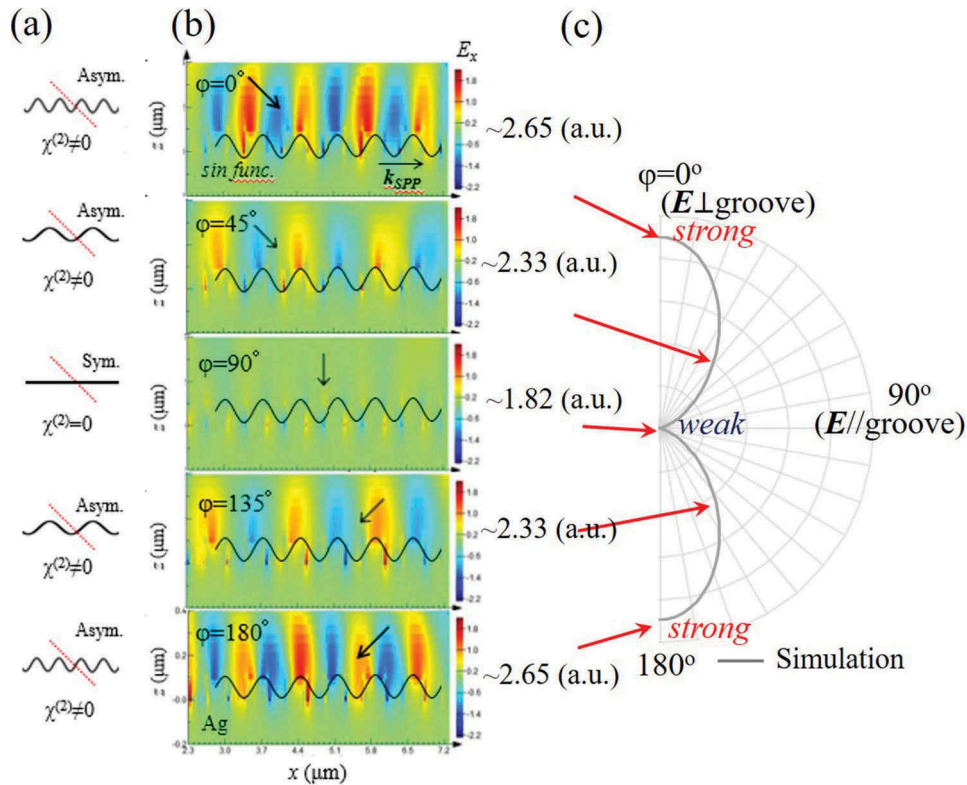
Figure 7. (a) The contribution of $\chi^{(2)}$ for the Ag sample at $\varphi = 0°$, 45°, 90°, 135°, and 180°. Dotted red lines indicate the mirror plane. (b) Electric field distributions for the 5.3-nm-thick SiO-coated Ag NC-LIPSSs calculated for configurations with $\theta = 45°$ and $\varphi = 0°$, 45°, 90°, 135°, and 180° using the FDTD method. The effective refractive index due to the nanostructures on top of the microgrooves, $\eta = 1.190$ for Ag, was used in this calculation. E_x is the x component of the E field. The red and blue color scales show positive and negative changes in optical density, respectively. $|E|$ is the electric field magnitude. The color scale bar indicates the electric field strength, and the values correspond to the absolute electric field intensity. The arrows indicate the wave vector k of an incident beam. (c) Simulated SHG intensity curves ranging from $\varphi = 0°$ to $\varphi = 180°$ for the sample rotation angle φ. The black curve is the theoretical intensity curve, described as $\{|\chi^{(2)}||E||E|\}^2$.

lower. This relationship provides the field enhancement curve as a function φ.

By using the χ induced by the structure's symmetry and the local field enhancement induced by SP, the expected intensity curve is represented as the black curve in Figure 7(c). The analysis method based on the relation between χ and the near field has been reported elsewhere [17,44]. The expected SHG curve is described as ranging from $\varphi = 0$ to $\varphi = 180$, so the whole simulation pattern for the SHG forms two lobes consisting of the modified $\cos^2(\varphi)$ function.

In fact, we measured the SHG as a function of the sample rotation angle φ from the NC-LIPSSs at $\theta = 45°$ using the setup shown in Figure 8(a). The sample rotation angle φ was defined as the angle between the incident plane and the sub-micro-groove direction (y-direction), or between the laser polarization and the **k** vector of the microgrooves. Figure 8(b) shows the SHG intensity for the Ag sample as a function of φ from the Ag NC-LIPSSs. Here, the SHG pattern in the p-in/p-out polarization configuration exhibited maxima at $\varphi = 0°$ and $180°$ ($E⊥$groove). We should notice that the experimental data fit relatively well to the simulated curve shown in Figure 8(b). The SHG intensity pattern for the p-in/p-out polarization combination depends strongly on the rotation angle φ, and it is clear that the intensity is sensitive not only to the symmetry of the sub-microgroove structure but also to local field enhancements.

However, the contribution from I_{SHG} with the NC-LIPSSs on the Ag does not completely reproduce our observed SHG intensity pattern, as seen in Figure 8(b). (Although SH radiation collected from nanometer-scale areas is strongly depolarized [45] and dephased [46], we did not consider these influences in the Ag sample.) This fact indicates that SHG in p-in/p-out polarization cannot be explained solely by propagating SPs on the microgrooves' surface.

Thus, we considered the nanostructural effects on the SHG intensity pattern. Extensive nanostructures from Figure 3(e) were observed on top of the LIPSSs. It is known that localized SPs can be generated from nanostructures [24,47,48], and the localized SPs, if they exist, may generate an isotropic SHG enhancement in the p-in/p-out polarization configuration. Here, we believe that the non-zero SHG components around $\varphi = 90°$ and $270°$ in Figure 8(b) arise from SHG enhancement due to the localized SPs. In addition, we suggest that the finite SHG on the Ag at other angles, as seen in Figure 3(e), is due to localized SP polariton excitation in nanostructures. In Figure 6, the difference between the generated SHG at $\varphi = 0°$ and $90°$ is very small at most angles. This is because the localized SPs in both conditions with incident electric field normal and parallel to the groove direction are excited. We believe that the SHG in Figure 3(b) is formed by the propagating and localized SPs from microgrooves and nanostructures.

In order to control the plasmonic enhancement effect of SHG, we tried to remove the nanostructural effect on the Ag sample. As shown in Figure 9(a) and Figure 9(c), there are many ablated nanodots, leading to isotropic SHG, by using setup of Figure 9(b), as seen in Figure 9(d). The sample was immersed in isopropanol and distilled water and cleaned for ~10 min with an ultrasonic cleaner after the creation of NC-LIPSSs to remove the nanostructures (NSs) on microgrooves. Figure 10(a) shows the SEM image of the obtained sample. A small amount of NS was removed; however, because the difference in surface quality before and after cleaning was very small, a smoother microgroove structure was not obtained. One reason, that SHG
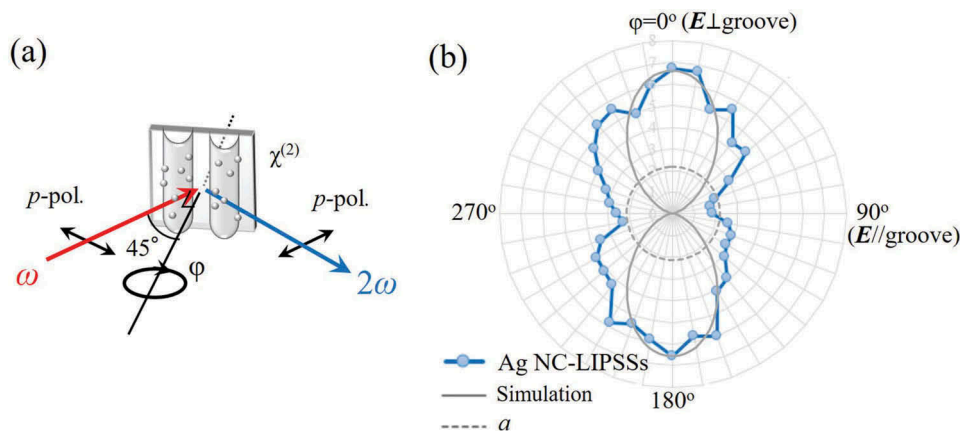

Figure 8. (a) Optical configuration of the reflected SHG intensity measurement for Ag sample at incidence angle θ. The sample rotation angle φ is defined as the angle between the incident plane and the groove direction. The laser polarization is indicated with a double arrow in the scheme. (b) The SHG intensity pattern of the NC-LIPSSs on Ag for p-in/p-out polarization configuration as a function of the sample rotation angle φ. The solid curves show the simulation curves calculated in Figure 7(c). The data points are connected by lines to guide the eye.
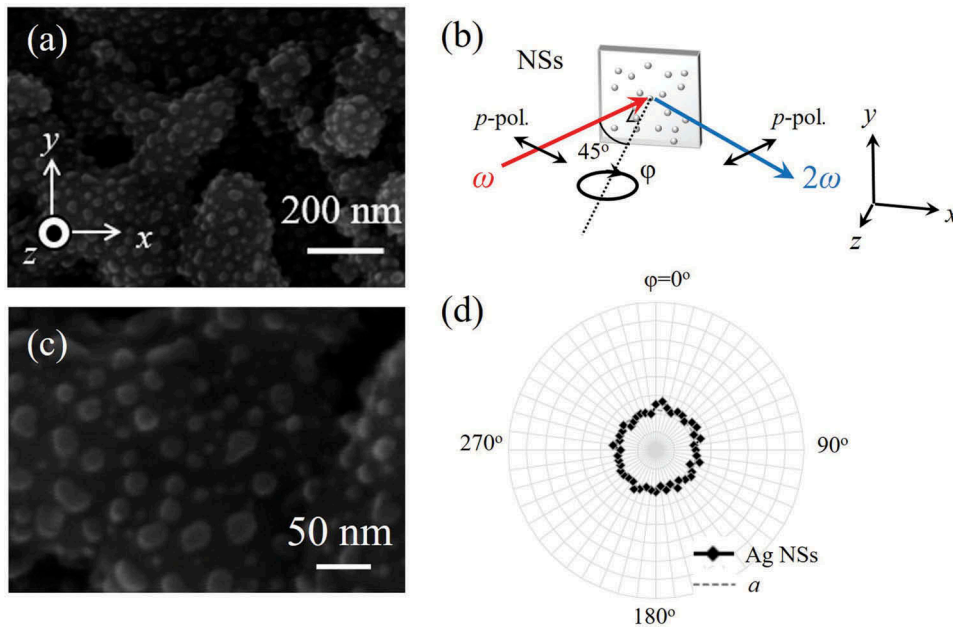
Figure 9. Nanostructural effects on the SHG intensity pattern. (a) The SEM image of the surface of a Ag NS sample, and (b) the expanding image. (c) Configuration of the NSs in the SHG intensity measurement. (d) The SHG intensity pattern of the NSs as a function of the sample rotation angle φ. The data points are connected by lines to guide the eye. The dotted circle shows the isotropic intensity pattern formed by averaged intensity.
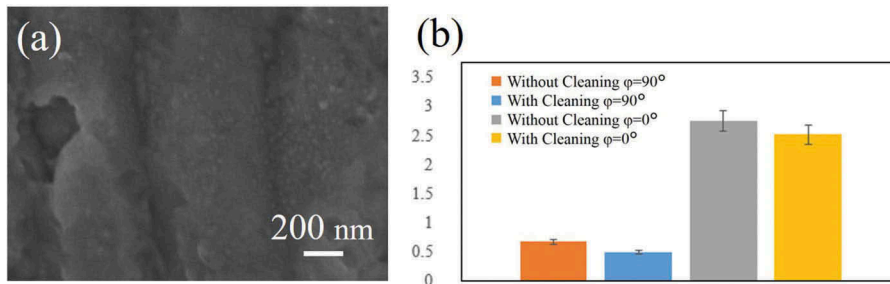
Figure 10. (a) SEM images of a Ag sample with cleaning. (b) SHG intensity for *p*-in/*p*-out polarization configuration at $\varphi = 0°$ and $\varphi = 90°$ with and without cleaning, respectively.

intensity at $\varphi = 0°$ and 90° did not show the difference before and after cleaning as shown in Figure 10(b), is plausible. Thus, to control the SHG intensity on the Ag sample, a more appropriate sample was required. In the next section, we shall select the Ni substrate as an appropriate medium.

3.2. SHG signal from Ni samples

As in the metallic groove sample, we first defined the relationship between the reflected SHG light $I(2\omega)$ and the nonlinear susceptibility $\chi^{(2)}$ of the metallic cube sample, as done in a previous study [17]. The *s*-polarized SHG intensity $|E_s(2\omega)|^2$ {= $I_s(2\omega)$} generated using the $\chi^{(2)}_{YYY}$ element is given as:

$$\left|E_s^R(2\omega)\right|^2 \propto \left|L_Y(2\omega)\chi^{(2)}_{YYY}E_{Y,\text{loc}}^2(\omega)\right|^2 \quad (3)$$

The local electric field E_{loc} has the relation $E_{\text{loc}} = L(\omega)E(\omega)$. Consequently, Equation (3) shows that the *s*-polarized SHG intensity $|E_s(2\omega)|^2$ depends on the local electric field E_{loc} of the *Y*-direction component.

3.2.1. Power dependence of the SHG from Ni NC-MCs

Figure 11 shows the excitation power dependence of the SHG signals measured on Ni NC-MCs. The data show that the SHG signal has a nearly quadratic depen-
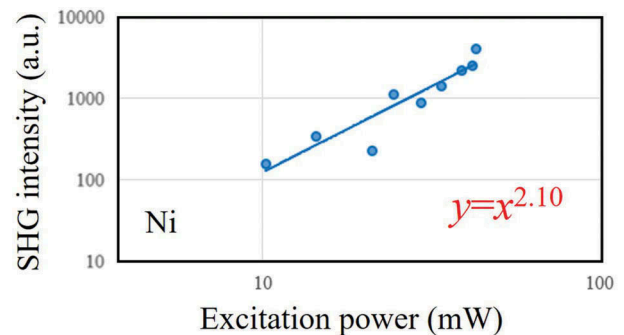
Figure 11. Excitation power dependence of the observed SHG intensity for the Ni NC-MCs plotted on a log–log scale. The slope value for the fits to these data is ~2, confirming the second-order nature of the emitting light.

dence on the excitation intensity (slope: 2.10), which indicates a characteristic of the second-order nonlinear processes. The conversion efficiency from fundamental to SHG light photons for the Ni sample was ~10^{-13} at the maxima for the s-in/s-out polarization configuration. The conversion efficiency of the Ni sample was somewhat weaker than that of the Ag sample.

3.2.2. Sample rotation angle dependence of the SHG from Ni NC-MCs

To investigate the origin of the anisotropic enhancement of the SHG, we analyzed the $\chi^{(2)}$ of the NC-MC surface of Ni. The $\chi^{(2)}$ is sensitive to the symmetry of the shape [5,6]. As indicated in Appendix 1, if we assume that the Ni microcubes (system: tetragon) have C_{4v} symmetry with four mirror planes, three nonlinear susceptibility elements, $\chi^{(2)}_{ZZZ}$, $\chi^{(2)}_{ZXX} = \chi^{(2)}_{ZYY}$, $\chi^{(2)}_{XZX} = \chi^{(2)}_{YZY} = \chi^{(2)}_{XXZ} = \chi^{(2)}_{YYZ}$, should be permitted. On the other hand, the $\chi^{(2)}$ element for the s-in/s-out polarization configuration should not appear. However, by considering mirror symmetry with respect to the φ change, the $\chi^{(2)*}_{YYY}$ panel is assumed to be newly induced, as illustrated in Figure 12(a). The candidate for this induced panel is that the symmetry of the microscopic shape indicates C_s symmetry lower than C_{4v} symmetry. If so, 10 independent nonlinear susceptibility elements should be permitted and thus real $\chi^{(2)}_{YYY}$ for the s-in/s-out polarization configuration should be accepted [2,5]. The other candidate is that the $\chi^{(2)}_{YYY}$ panel can be induced under C_{4v} symmetry in a specific configuration [17], or the shape of the microcubes has broken symmetry at the air–metal interface [24]. However, the consideration of the E field of the incident light being converted from s- to p-polarization by a polarization scrambling effect [6,45] is plausible as one of the candidates.

Thus, we assume that the E field of the incident light being converted from s- to p-polarization is due to the polarization scrambling effect originating from the surface nano-roughness, namely the conversion of the s-polarized incident field of frequency ω by the roughness $\zeta(x, y)$, as illustrated in Figure 13. Ogata et al. [6] have discussed the general effect of the roughness of the metallic nanowire's surfaces on the optical process upon them. Using their formalism, we consider the conversion of s-polarized light into p-polarized light due to the roughness of the nanowire structure used here. We consider the conversion of the s-polarized incident field of frequency x by the roughness $\zeta(x, y)$ of the metal cube structure. Here, $\zeta(x, y)$ represents the deviation of the height of the metal surface of the microcube from that of the ideal. We consider the case of $\varphi = 0°$ so that the wave vector component of the incident light parallel to the substrate is in direction x. The electric field of the s-polarized incident light is in direction y. The electric field,

E^{ω}_{NF}, near the microcube is generally expanded with respect to $\zeta(x, y)$ as:

$$\vec{E}^{\omega}_{NF} = E^{\omega}_Y \vec{e}_Y + \varsigma(x,y)(c^{(1)}_{YX}\vec{e}_X + c^{(1)}_{YZ}\vec{e}_Z)E^{\omega}_Y$$
$$+ \varsigma(x,y)^2(c^{(2)}_{YX}\vec{e}_X + c^{(2)}_{YZ}\vec{e}_Z)E^{\omega}_Y \quad (4)$$

Here, $C^{(i)}_{jk}$ is a coefficient describing the rate of the conversion of the j-polarized electric field into the k-polarized one, and $\vec{e}_X$ and $\vec{e}_Y$ are unit vectors in the X- and Y- directions, respectively. Averaging Equation (4) over the area on the substrate of a wavelength size, the second term vanishes and Equation (4) becomes:

$$\langle \vec{E}^{\omega}_{NF} \rangle = E^{\omega}_Y \vec{e}_Y + \varsigma(x,y)^2(c^{(2)}_{YX}\vec{e}_X + c^{(2)}_{YZ}\vec{e}_Z)E^{\omega}_Y \quad (5)$$

since $\zeta(x, y)$. Hence, the third component of the averaged electric field is

$$\langle \vec{E}^{\omega}_{NF,Z} \rangle = \varsigma(x,y)^2 c^{(2)}_{YZ} E^{\omega}_Y \quad (6)$$

Here, we suggest that the contribution of $\chi^{(2)}_{YYZ}$ was primarily responsible for the enhancement of the SHG intensity, as expected in Figure 12(a). This nonlinear susceptibility element gives a nonlinear polarization:

$$P^{NL}_Y = \varepsilon_0 L^{2\omega}_Y \chi^{(2)}_{YYZ} E^{\omega}_Y L^{\omega}_Y E^{\omega}_Z L^{\omega}_Z \quad (7)$$

Substituting the third component of Equation (6) for E^{ω}_Z in Equation (7), we obtain

$$P^{NL}_Y = \varepsilon_0 L^{2\omega}_Y \chi^{(2)}_{YYZ} E^{\omega}_Y L^{\omega}_Y \langle E^{\omega}_{NF,Z} \rangle L^{\omega}_Z$$
$$= \varepsilon_0 L^{2\omega}_Y \chi^{(2)}_{YYZ} E^{\omega}_Y L^{\omega}_Y \langle \varsigma(x,y)^2 \rangle c^{(2)}_{YZ} E^{\omega}_Y L^{\omega}_Z \quad (8)$$

Equation (8) indicates that the roughness on the microcube generates SHG in the s-in/s-out polarization configuration at $\varphi = 0$. If $E^{\omega}_{NF,Z}$ depends weakly on the direction of the incident electric field, the SHG intensity generated by Equation (8) in s-in/s-out should be as follows:

$$I^{2\omega}_s \propto \left| L^{2\omega}_Y \chi^{(2)}_{YYZ} E^{\omega 2}_Y L^{\omega 2}_Y \sin^2(4\phi) \right|^2 \quad (9)$$

Here, $\chi^{(2)}_{YYZ}$ is non-zero under C_{4v} symmetry. Therefore, Equation (9) is large when the incident electric field is in direction y. In this configuration, the pattern exhibits eight lobes at the minima with $\varphi = 0°, 45°, 90°, 135°, 180°, 225°, 270°$, and $315°$, as seen in Equation (9). Hence, if we consider the polarization scrambling effect, the formation of a SHG pattern with eight lobes can be explained. Namely, if we assume that the contribution of $\chi^{(2)}_{YYZ}$ is effective for the s-in/s-out polarization configuration in this work, the SHG intensity should be zero at $\varphi = 0°$, 45°, and 90° ranging from $\varphi = 0°$ to $\varphi = 90°$, as shown in Figure 12(a). In conclusion, the $\chi^{(2)}_{YYZ}$ depending on a $\sin(4\varphi)$ function dominates the SHG
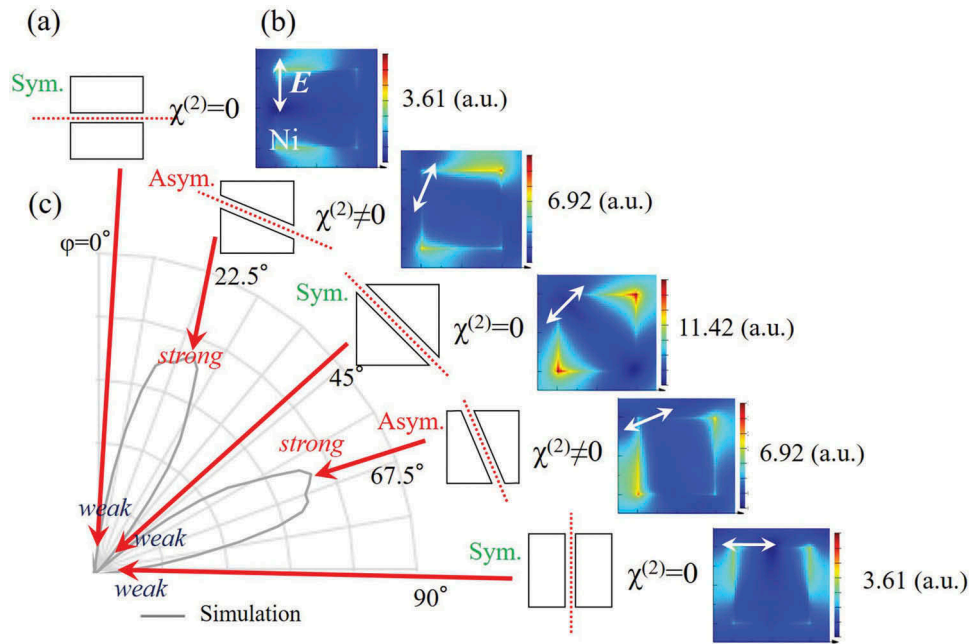
Figure 12. SHG enhancement. (a) The contribution of $\chi^{(2)}$ for the Ni sample at $\varphi = 0°$, 22.5°, 45°, 67.5°, and 90°. Red dotted lines indicate the mirror plane. (b) Electric field distributions for the Ni NC-MCs calculated for the configurations at an incidence angle of 45° and $\varphi = 0°$, 22.5°, 45°, 67.5°, and 90° by using the FDTD method, and an enhancement factor (EF) curve for the sample rotation angle φ. The effective refractive index due to the nanostructures on top of the microgrooves, $\eta = 1.333$ for the Ni sample, was used in this calculation. $|E|$ is the electric field magnitude. The color scale bar indicates the electric field strength and the values show the local electric field magnitude. Double arrows indicate the electric field vector $\boldsymbol{E}$ of an incident beam. Blue dotted curve represents EFs consisting of the $|E|^2$ values calculated by using the FDTD method. (c) Simulated SHG intensity curves for the sample rotation angle φ. The red curve is the theoretical intensity curve, described as $\{|\chi^{(2)}|\|E\|\|E\|\}^2$.

intensity from the NC-MCs on Ni. Thus, the symmetry for the Ni NC-MCs was fitted by $\sin^2(4\varphi)$.

The NC-MCs in this study were created using a normal incident beam. In this case, the periodicity Λ of the surface grating formed by interference between the incident laser light and the excited SP wave is given by Equation (2), as well as in the Ag case. For the smooth Ni samples, the periodicity of the grooves Λ was calculated as $\varepsilon_{Ni}' = -13.0$ for the Ni [43]. By using Equation (2), Λ was found to be 769 nm for the Ni sample. However, the observed Λ was about 600 nm for the Ni sample, as observed in Figure 3(f). By using this observed Λ value, we found that $\varepsilon_{Ni}' = -4.00$ for the Ni sample. This effective dielectric constant might arise from the NSs on top of the microstructures [27]. Using this effective dielectric constant, we next investigated the electric field distribution at an incidence angle of 45° on a periodic cube surface on the Ni sample.

Likewise, to find the origin of the enhanced SHG, we next calculated the local electric field E_{loc} intensity on the sample using the FDTD method. The electric field distribution from $\varphi = 0°$ to $\varphi = 90°$ is shown in Figure 12(b). The color scale bar indicates the electric field magnitude $|E|$. Sharper metal tips can produce strong local electromagnetic fields, called the lightning rod effect. Recently, studies have reported the lightning rod effect induced at the tips at the Ni nanostructure for the s-in/s-out polarization

configuration [49]. Thus, the lightning rod effect should be induced at the edge parts of the Ni sub-microcube structures. In Figure 12(b), the enhancement of the local electric field E_{loc} at the edge parts is clearly seen, and this enhancement is led by the lightning rod effect. The value in Figure 12(b) indicates the maximal electric field magnitude $|E_{loc}|_{max}$ in the simulation. At $\varphi = 45°$, the value of $|E_{loc}|_{max}$ was higher, and at $\varphi = 0°$ and 90°, the values of $|E_{loc}|_{max}$ were lower. This relationship provides the field enhancement curve as a function φ.

Using the χ induced by the structure's symmetry and the local field enhancement induced by SP, the expected intensity curve is represented as the black curve in Figure 7(c). The expected SHG curve is described as ranging from $\varphi = 0°$ to $\varphi = 90°$ so that the whole simulation pattern for the SHG forms eight lobes consisting of the modified $\sin^2(4\varphi)$ function.

We observed the azimuthal angular dependence of the SHG from NC-MCs at an incidence angle of 45°, as shown in Figure 14(a). Here, 45° incidence is appropriate for defining nonlinear polarization with third-rank tensors. For example, when $\theta = 0°$, the component for the z-direction does not exist; therefore, the nonlinear polarization should be defined using x- and y-directions only, as such small amounts of information do not play a role in χ analysis. When $0° < \theta < 45°$ and $45° < \theta < 90°$, the nonlinear polarization should be defined by modifying the information for the beam-
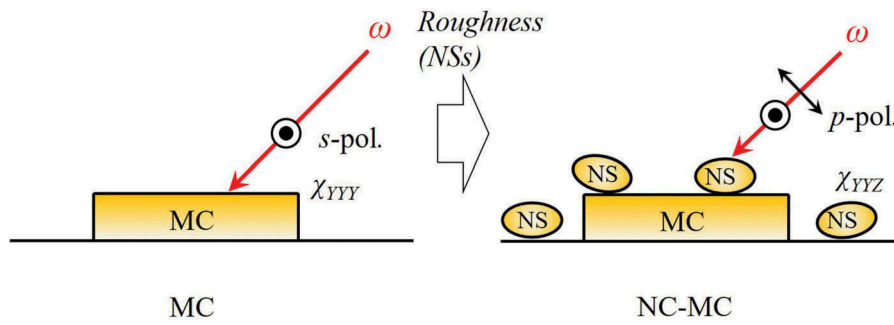
Figure 13. Polarization scrambling effect induced by the roughness of nanostructures.

spot size and E field/wave vector(s) on a case-by-case basis; thus, χ analysis may be complicated. The design of a 45° incidence with a large volume of information and an easier understanding is valid for the experiments. The sample rotation angle φ was defined as the angle between the incident plane and the sub-microgroove direction (x- or y-direction). Figure 14(b) illustrates the SHG intensity in the s-in/s-out polarization configuration for the Ni sample as a function of the sample rotation angle φ from the Ni NC-MCs. The simulated curve in Figure 12(c) is patterned in Figure 14(b). In fact, the SHG pattern in the s-in/s-out polarization configuration exhibited eight dim minima at $\varphi = 0°$, 45°, 90°, 135°, 180°, 225°, 270°, and 315°. Thus, the SHG intensity pattern for the s-in/s-out polarization combination strongly depends on the rotation angle φ, and it was clear that the intensity is sensitive not only to the symmetry parameter but also to the enhancement factor (EF) of the electric field. Namely, when the structure gives the largest near-field enhancement, the smallest SHG signal is provided both in the $\sin^2(4\varphi)$ model and in the SHG

data due to the symmetry-selection properties of SHG. On the other hand, the nano/micro-hierarchical structure consisting of structures with different sizes may induce cascaded plasmon field enhancement [50]. If the nanostructures are in contact with the corners of microcube structures as seen in Figure 15(a,b), a large local field enhancement will be obtained by the cascading field enhancement effect originating from the 'lightning rod' effect. Then, the E field concentration might boost the finite SHG intensity at the azimuthal angle φ without mirror symmetry.

Figure 14(b) also reveals, however, a non-zero SHG intensity at $\varphi = 0°$, 45°, 90°, 135°, 180°, 225°, 270°, and 315°, and the contribution from I_{SHG} with the NC-MCs on the Ni does not completely reproduce our observed SHG intensity pattern, as seen in Figure 14 (b). This fact indicates that SHG in s-in/s-out polarization cannot be explained solely by the symmetry and SPs on the microcube-structured surface.

Here, we merely comment on the contribution of the quadrupolar effect [51] in our SHG signals. Then, what is the quadrupolar effect? We should note that
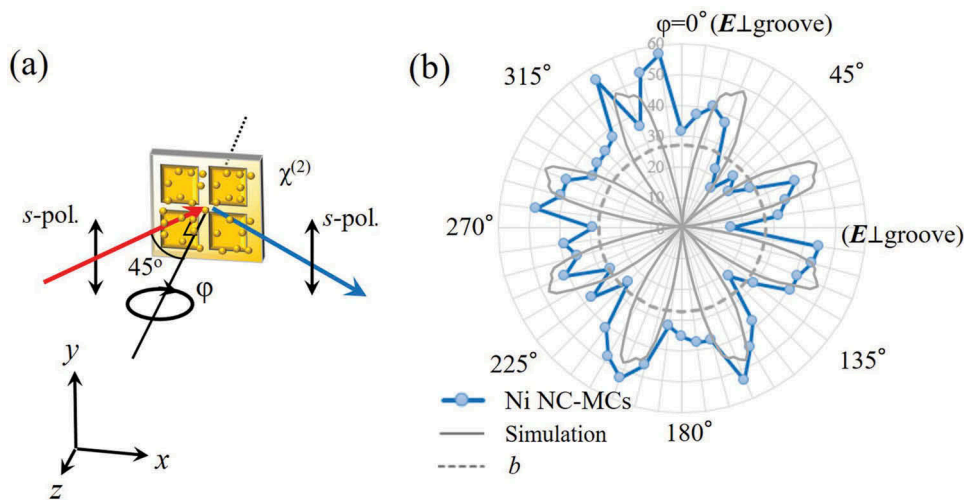
Figure 14. Angular SHG intensity. (a) Optical configuration of the reflected SHG intensity measurement for a Ag sample at incidence angle θ. The sample rotation angle φ is defined as the angle between the incident plane and the groove direction. The laser polarization is indicated with a double arrow in the scheme. (b) The SHG intensity pattern of the NC-MCs as a function of the sample rotation angle φ. The data points are connected by lines to guide the eye. The solid curve shows the simulation curve calculated in Figure 12(c). The dotted lines show the isotropic intensity pattern formed by averaged intensity at $\varphi = 0°$, 45°, 90°, 135°, 180°, 225°, 270°, and 315°.

the nonlinear polarization P^{NL} includes a dipole and a quadrupole. The nonlinear polarization P^{NL} including the quadrupole is written as:

$$\vec{P}_i(2\omega) = \varepsilon_0 \chi_{ijk}^D \vec{E}_j(\omega)\vec{E}_k(\omega) + \varepsilon_0 \chi_{ijkl}^Q \vec{E}_j(\omega)\nabla_k\vec{E}_l(\omega) \quad (10)$$

Here, superscripts D and Q indicate the electric dipole and quadrupole, and χ_{ijk} and χ_{ijkl} indicate third- and fourth-rank tensor, respectively. The fourth-rank tensor shows a finite value even for centrosymmetric systems. In general, the bulk crystal in which the fluctuation of the electric field is smoother than the wavelength can be disregarded; meanwhile, the thin film or part with a large contribution to the surface and interface cannot be disregarded. In this work, the SHG intensity for s-in/s-out polarization from a smooth Ni bulk sample was at the noise level, as we found in a separate experiment. This implies that the electronic quadruple effect from the Ni bulk sample can be disregarded. On the contrary, the SHG from Ni NC-MCs with nanometer thickness generally includes both dipole and electronic quadruple effects. Dipolar SHG originating from the third-rank tensor is sensitive to the asymmetry of the structure, while quadrupolar SHG originating from the fourth-rank tensor is insensitive to it. In Figure 14(b), the angular SHG patterns observed from Ni NC-MCs shows sensitive dependence on the asymmetry of the microstructures. Therefore, it is suggested that the quadrupolar effect for s-in/s-out polarization is not dominant, namely $\chi_{YYYY}E_Y\nabla_Y E_Y \fallingdotseq 0$. (In this work, since the magnetic field is not applied, the magnetically induced nonlinear optical effect [17,52] is disregarded.)

Thus, we considered the nanostructural effects on the SHG intensity pattern as observed in Figure 14(b). Extensive NSs from Figure 3(f) were observed on top of the MCs. It is known that localized SPs can be generated from NSs [47], and the localized SPs, if they exist, may generate an isotropic SHG enhancement in s-in/s-out polarization configurations. To clarify this, we additionally produced NSs on Ni using the technique shown in Figure 2(b) and measured their

SHG as a function of rotation angle φ using the setup shown in Figure 4. Figure 16(a) shows the NSs induced on Ni by performing ablation at a laser fluence of 50.0 mJ/cm^2 using the setup illustrated in Figure 16(c). Most of the structures were nanodots with a diameter in the range of 5–80 nm, as seen in Figure 16(b). In the SHG measurement, we observed isotropic SHG enhancement from NSs on Ni in the s-in/s-out polarization configuration, as shown in Figure 16(d). Thus, we can say that the non-zero SHG components around $\varphi = 0°$, 45°, 90°, 135°, 180°, 225°, 270°, and 315° in Figure 14(b) arise from SHG enhancement due to the localized SPs on the NSs. We found that the SHG in Figure 14(b) is formed by the excitation of SPs from both MCs and NSs.

To control the plasmonic enhancement effect of SHG, we tried to remove the nanostructural effect on the Ni sample. As shown in Figure 3(f), there are many ablated nanodots on microcubes, leading to isotropic SHG, as seen in Figure 16(d). The sample was immersed in isopropanol and distilled water and cleaned for ~10 min with an ultrasonic cleaner after the creation of NC-MCs to remove the NSs on microcubes. By doing so, the microcubes become much cleaner. The SEM images of the surface of the obtained MC sample are shown in Figure 17(a,b). We next measured their SHG signal, as shown in Figure 17 (c). Figure 17(d) shows the SHG intensity pattern in s-in/s-out polarization configuration for MCs on the Ni sample. The pattern clearly exhibited eight lobes at the minima with $\varphi = 0°$, 45°, 90°, 135°, 180°, 225°, 270°, and 315°, and the minimal intensity ('b' in Figure 17 (d)) was approximately ~34.7% lower than that for the NC-MCs ('a' in Figure 14(b)). Together, these findings indicate that NSs could not be completely removed, but the isotropic SHG emission from the NSs was suppressed with decreasing amounts of NSs. We expect that the nanostructure-covered microstructures make the polarization scrambling effect small with a decreasing amount of nanostructures. If so, the SHG pattern with eight lobes for the MC structure seems to be small and the total SHG pattern seems to
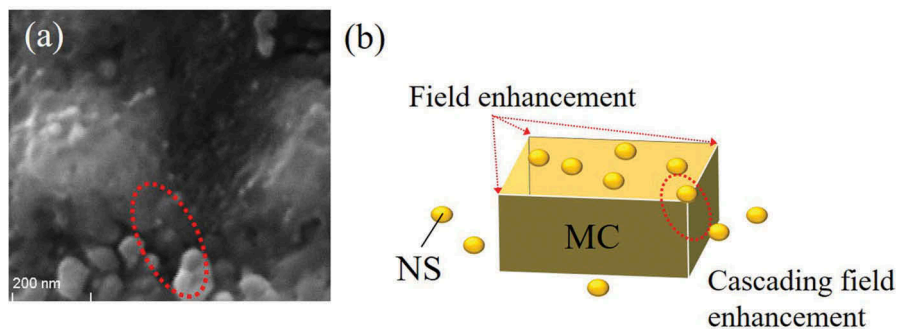
Figure 15. Cascading field enhancement effect. (a) The expanded SEM image when the nanostructure is in contact with the corner of a microcube structure and (b) their representation. A large local field enhancement might be obtained by the cascading field enhancement effect where indicated in the red dotted circle.
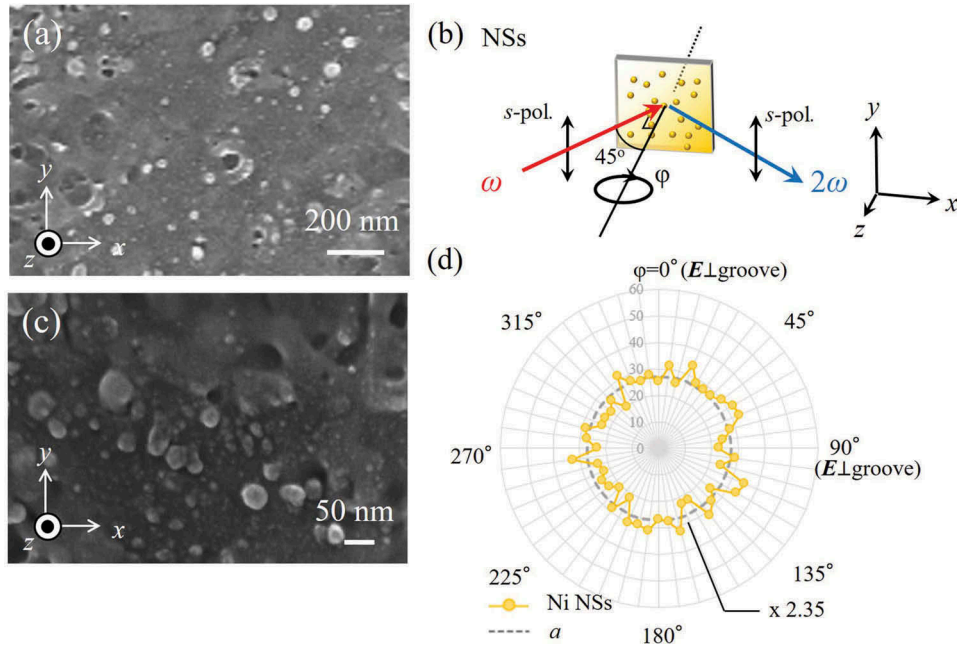
Figure 16. Nanostructural effects on the SHG intensity pattern. (a) The SEM image of the surface of a Ni NS sample, and (b) the expanding image. (c) Configuration of the NSs in the SHG intensity measurement. (d) The SHG intensity pattern of the NSs as a function of the sample rotation angle φ. The data points are connected by lines to guide the eye. The dotted circle shows the isotropic intensity pattern formed by averaged intensity.

be large and circular. However, the measured SHG seen in Figure 17(d) is formed by the large eight lobes and a small circle. This means 'the polarization scrambling effect relates to nanostructure better than the localized SP effect'. The incomplete removal of NSs makes the behavior of SHG complicated.

Incidentally, to remove NSs perfectly, laser irradiation was also tested on the Ni surface at normal incidence in water [42] using the experimental setup shown in Figure 2(b). However, as seen in Figure 17 (e,f), we could neither remove the NSs nor fabricate the cube structures. Unremoved NS is due to the dramatic change of the dielectric for the metal–water interface by performing the laser ablation in water. According to the SEM image, the periodicity of broken cubes was 300 nm. Considering this, if we calculate the dielectric for the metal–water interface using $\varepsilon_{Ni}' = -4.00$ in Equation (7), it is determined to be $\varepsilon_d' = 2.56$. This fact shows a large quantitative change from $\varepsilon_d' = 1.00$ to $\varepsilon_d' = 2.56$. On the other hand, regarding why the cube sample cannot be created, plasma generation in water is a plausible explanation. In any case, the sample obtained by laser ablation in water is not appropriate for our SHG experiment, and thus is excluded from our work.

Returning to the main topic. How many NSs could be removed by the cleaning method? According to quantitative analysis, the existence probability of NSs on NC-MCs was found to be 11.71% of the whole surface seen in Figure 3(h). On the other hand, the existence probability of NSs on MCs was found to be 2.65% of the whole surface seen in Figure 14(a).

Namely, we can thus say that 9.06% of the NSs on the whole surface was removed.

In fact, however, most of the nanostructures were removed, as seen in Figure 17(a). Although most of the nanostructures were removed, it is not entirely clear why the minimum intensities in the pattern do not show a large reduction. Thus, we considered the dephasing of the light field induced by the NSs on the Ni microstructures seen in Figure 17(a). In general, SH radiation collected from nanometer-scale areas is strongly dephased [53]. Stockman [46] has discussed the dephasing effect in terms of the roughness of metal surfaces on the optical processes upon them. Based on their theorem, we considered the propagating delay of fundamental light by the roughness on a nanoscale.

The origin of the dephasing is the delocalization of the linear local field [46]. The actual delocalization of the nanoscale optical fields induced in the Ni surface causes their concentration areas (i.e. hot spots) to overlap for different propagations. Since these propagating modes have randomly different frequencies, this leads to random phase shifts and results in dephasing [46]. More materially, the timing of the penetration of the propagating light is off when the NSs exist on a surface, resulting in dephasing. Namely, when the incident wave comes to a MC structure with NSs as illustrated in Figure 18(a), the hit-part of the wave to material is slightly different from an ideal MC structure, as illustrated in Figure 18 (b), due to the existence of NSs. As a result, a random phase shift in the incident wave, called dephasing by propagation delay, occurs. The dephasing may cause
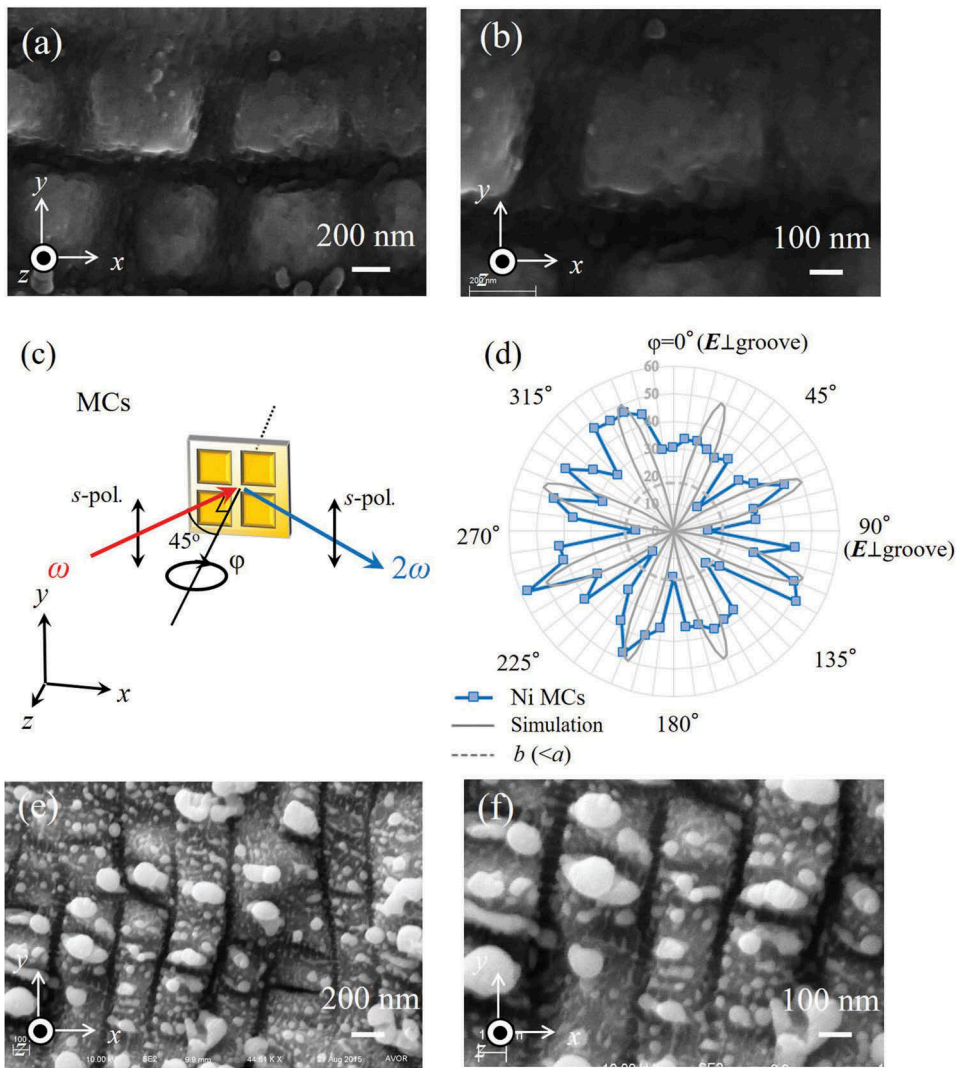
Figure 17. Effect of NSs on SHG emission. (a) The SEM image of the surface of a Ni MC sample. (b) The expanded image of (a). (c) Configuration of the MCs in the SHG intensity measurement. (d) The SHG intensity pattern of the MCs as a function of the sample rotation angle φ. The data points are connected by lines to guide the eye. The solid curve shows the simulation curve calculated using $\eta = 1.041$ in Figure 3(c). The dotted line shows the isotropic intensity pattern formed by averaged intensity at $\varphi = 0°$, 45°, 90°, 135°, 180°, 225°, 270°, and 315°. (e) The SEM image of the surface of Ni created by laser-treating in water, and (f) its expanded image.
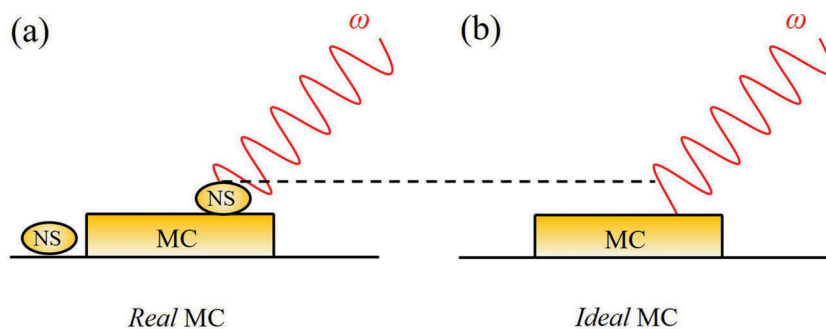
Figure 18. Dephasing of the SHG on surfaces. A timing of the penetration of the propagating light on (a) real and (b) ideal MC surfaces.

noise in the intensity data. Therefore, we concluded that the SHG pattern in Figure 17(d) may contain noise due to the dephasing at rotation angle φ under forbidden conditions.

4. Conclusions

We have systematically analyzed the SHG intensity from the constituted NC-LIPSSs and NC-MC hierarchical surface structures on metals. We observed unique

anisotropic SHG enhancements causing symmetry of shapes and excitation of SPs. The SHG patterns are attributed to the localized/propagating and localized/localized SPs on nano/micro-surface structures on Ag and Ni, respectively. The contribution of microstructure to SHG was found to be larger than that of nanostructure. Furthermore, the separation of nano/microstructure related to the decomposition of the SHG intensity patterns. Left SHG was explained by the dephasing effect of propagating delay. These interesting physical phenomena can find possible applications in novel symmetry-sensitive plasmon optical devices.

Acknowledgments

Disclosure statement

No potential conflict of interest was reported by the authors.

Notes on contributors

Yoichi Ogata is an Enterprise Cooperation Researcher at the Center for Advanced Photonics at RIKEN. His research is in the area of nanotechnology and nonlinear optics. He received his PhD in Materials Science from the Japan Advanced Institute of Science and Technology. He worked for several years as a Project Assistant Professor at the Tokyo University of Agriculture and Technology in the Department of Applied Physics, Visiting Research Associate and then later on as Research Associate with the University of Rochester in the Institute of Optics. He brought to the table his passion for studying and teaching at a university level 'Nonlinear Optics of Metallic Nano and/or Micro structures' as it has been a primary focus of his career. Specifically, he has developed an expertise in second-harmonic generation spectroscopy and nanofabrication. He has had more than 10 papers published in international journals.
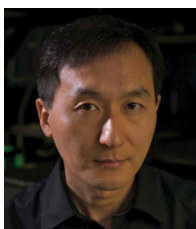
Chunlei Guo is a Professor in The Institute of Optics and Department of Physics and Astronomy at the University of Rochester. His research is in the area of femtosecond lasermatter interactions. He received his PhD in Physics from the University of Connecticut and postdoctoral training at the Los Alamos National Laboratory. His work at Rochester has led to the discoveries of a range of highly functionalized materials, which may find a broad range of applications and have been featured extensively by the media, including four *New York Times* features. He is a Fellow of the American Physical Society and Optical Society of America. Currently, he serves as the Editor-in-Chief for one of the most widely used handbooks in lasers and optics, *CRC Handbook of Laser Technology and Applications* (2nd Edition).

References

[1] Liu S, Sinclair MB, Saravi S, et al. Resonantly enhanced second-harmonic generation using III–V semiconductor all-dielectric metasurfaces. Nano Lett. 2016;16(9):5426–5432.

[2] Boyd RW. Nonlinear optics. 3rd ed. Amsterdam: Elsevier Inc; 2008.

[3] Shen YR. The principles of nonlinear optics. New York: J. Wiley & Sons; 1984.

[4] Johnson JC, Yan H, Schaller RD, et al. Near-field imaging of nonlinear optical mixing in single zinc oxide nanowires. Nano Lett. 2002;2(4):279–283.

[5] Ogata Y, Anh Tuan N, Miyauchi Y, et al. Optical second harmonic generation from Pt nanowires with boomerang-like cross-sectional shapes. J Appl Phys. 2011;110(4):044301.

[6] Ogata Y, Tuan NA, Takase S, et al. Polarization and azimuthal angle dependence of the optical second harmonic generation from Pt nanowires on the MgO (110) faceted template. Surf Interface Anal. 2010;42(10-11):1663–1666.

[7] Holmberg VC, Bogart TD, Chockla AM, et al. Optical properties of silicon and germanium nanowire fabric. J Phys Chem C. 2012;116(42):22486–22491.

[8] Liu ZW, Wei QH, Zhang X. Surface plasmon interference nanolithography. Nano Lett. 2005;5(5):957–961.

[9] Chen R, Crankshaw S, Tran T, et al. Second-harmonic generation from a single wurtzite GaAs nanoneedle. Appl Phys Lett. 2010;96(5):051110.

[10] Zhang Y, Grady NK, Ayala-Orozco C, et al. Three-dimensional nanostructures as highly efficient generators of second harmonic light. Nano Lett. 2011;11(12):5519–5523.

[11] Das SK, Bock M, O'Neill C, et al. Efficient second harmonic generation in ZnO nanorod arrays with broadband ultrashort pulses. Appl Phys Lett. 2008;93(18):181112.

[12] Ogata Y, Mizutani G. Absolute second order nonlinear susceptibility of Pt nanowire arrays on MgO faceted substrates with various cross-sectional shapes. Appl Phys Lett. 2013;103(9):093107.

[13] Lesuffleur A, Kumar LK, Gordon R. Enhanced second harmonic generation from nanoscale double-hole arrays in a gold film. Appl Phys Lett. 2006;88(26):261104.

[14] Farias GA, Maradudin AA. Second-harmonic generation in reflection from a metallic grating. Phys Rev B. 1984;30(6):3002.

[15] Lee KJ, Parmigiani F, Liu S, et al. Phase sensitive amplification based on quadratic cascading in a periodically poled lithium niobate waveguide. Opt Express. 2009;17(22):20393–20400.

[16] Foster MA, Turner AC, Lipson M, et al. Nonlinear optics in photonic nanowires. Opt Express. 2008;16(2):1300–1320.

[17] Valev VK, Silhanek AV, Gillijns W, et al. Plasmons reveal the direction of magnetization in nickel nanostructures. ACS Nano. 2010;5(1):91–96.

[18] Piccione B, Aspetti CO, Cho CH, et al. Tailoring light–matter coupling in semiconductor and hybrid-plasmonic nanowires. Rep Prog Phys. 2014;77(8):086401.

[19] Stockman MI, Bergman DJ, Anceau C, et al. Enhanced second-harmonic generation by metal surfaces with nanoscale roughness: nanoscale dephasing, depolarization, and correlations. Phys Rev Lett. 2004;92(5):057402.

[20] Link S, El-Sayed MA. Spectral properties and relaxation dynamics of surface plasmon electronic oscillations in gold and silver nanodots and nanorods. Phys Chem B. 1999;103(40):8410–8426.

[21] Quail JC, Simon HJ. Second-harmonic generation from a silver grating with surface plasmons. JOSA B. 1988;5 (2):325–329.

[22] Pipino AC, Van Duyne RP, Schatz GC. Surface-enhanced second-harmonic diffraction: experimental investigation of selective enhancement. Phys Rev B. 1996;53 (7):4162.

[23] Baida H, Mongin D, Christofilos D, et al. Ultrafast nonlinear optical response of a single gold nanorod near its surface plasmon resonance. Phys Rev Lett. 2011;107 (5):057402.

[24] Hubert C, Billot L, Adam PM, et al. Role of surface plasmon in second harmonic generation from gold nanorods. Appl Phys Lett. 2007;90(18):181105.

[25] Vorobyev AY, Guo C. Effects of nanostructure-covered femtosecond laser-induced periodic surface structures on optical absorptance of metals. Appl Phys A Mater Sci Process. 2007;86(3):321–324.

[26] Vorobyev AY, Makin VS, Guo C. Periodic ordering of random surface nanostructures induced by femtosecond laser pulses on metals. J Appl Phys. 2007;101 (3):034903.

[27] Hwang TY, Vorobyev AY, Guo C. Surface-plasmon-enhanced photoelectron emission from nanostructure-covered periodic grooves on metals. Phys Rev B. 2009;79(8):085425.

[28] Raether H. Surface plasmons on smooth and rough surfaces and on gratings. Berlin Heidelberg: Springer-Verlag; 1988.

[29] Walsh GF, Dal Negro L. Enhanced second harmonic generation by photonic–plasmonic Fano-type coupling in nanoplasmonic arrays. Nano Lett. 2013;13(7):3111–3117.

[30] Linnenbank H, Grynko Y, Förstner J, et al. Second harmonic generation spectroscopy on hybrid plasmonic/dielectric nanoantennas. Light Sci Appl. 2016;5(1):e16013.

[31] Gopinath A, Boriskina SV, Premasiri WR, et al. Plasmonic nanogalaxies: multiscale aperiodic arrays for surface-enhanced Raman sensing. Nano Lett. 2009;9 (11):3922–3929.

[32] Butet J, Duboisset J, Bachelier G, et al. Optical second harmonic generation of single metallic nanoparticles embedded in a homogeneous medium. Nano Lett. 2010;10(5):1717–1721.

[33] Luong N, Cheng CW, Shih MH, et al. Phase matching for surface plasmon enhanced second harmonic generation in a gold grating slab. Appl Phys Lett. 2012;100 (18):181107.

[34] Ogata Y, Vorobyev A, Guo C. Symmetry-sensitive plasmonic enhancement of nonlinear optical intensity in nano-micro hierarchical structures on silver. Surf Interface Anal. 2016;48(11):1108–1113.

[35] Ogata Y. Optical second harmonic generation from nanostructure-covered micro-cubes on nickel. Opt Mater Express. 2016;6(5):1520–1529.

[36] Huang M, Zhao FL, Jia TQ, et al. A uniform 290 nm periodic square structure on ZnO fabricated by two-beam femtosecond laser ablation. Nanotechnology. 2007;18(50):505301.

[37] Hollis DB. Review of hyper-Rayleigh and second-harmonic scattering in minerals and other inorganic solids. Am Mineralogist. 1988;73(7–8):701–706.

[38] Gomopoulos N, Lütgebaucks C, Sun Q, et al. Label-free second harmonic and hyper Rayleigh scattering with high efficiency. Opt Express. 2013;21(1):815–821.

[39] Vance FW, Lemon BI, Hupp JT. Enormous hyper-Rayleigh scattering from nanocrystalline gold particle suspensions. J Phys Chem B. 1998;102(50):10091–10093.

[40] Hao EC, Schatz GC, Johnson RC, et al. Hyper-Rayleigh scattering from silver nanoparticles. J Chem Phys. 2002;117(13):5963–5966.

[41] Campo J, Desmet F, Wenseleers W, et al. Highly sensitive setup for tunable wavelength hyper-Rayleigh scattering with parallel detection and calibration data for various solvents. Opt Express. 2009;17(6):4587–4604.

[42] Kuladeep R, Dar MH, Deepak KL, et al. Ultrafast laser induced periodic sub-wavelength aluminum surface structures and nanoparticles in air and liquids. J Appl Phys. 2014;116(11):113107.

[43] Ordal MA, Long LL, Bell RJ, et al. Optical properties of the metals al, co, cu, au, fe, pb, ni, pd, pt, ag, ti, and w in the infrared and far infrared. Appl Opt. 1983;22 (7):1099–1119.

[44] Tuan NA, Mizutani G. Metal-interface second harmonic generation from Pt/Cu bimetallic nanowire arrays on NaCl (110) faceted templates. E-J Surf Sci Nanotechnol. 2009;7:831–835.

[45] Maradudin AA, Mills DL. Scattering and absorption of electromagnetic radiation by a semi-infinite medium in the presence of surface roughness. Phys Rev B. 1975;11 (4):1392.

[46] Stockman MI. Giant fluctuations of second harmonic generation on nanostructured surfaces. Chem Phys. 2005;318(1):156–162.

[47] Lamprecht B, Leitner A, Aussenegg FR. SHG studies of plasmon dephasing in nanoparticles. Appl Phys B Lasers Opt. 1999;68(3):419–423.

[48] Li K, Stockman MI, Bergman DJ. Enhanced second harmonic generation in a self-similar chain of metal nanospheres. Phys Rev B. 2005;72(15):153401.

[49] Valev VK, Zheng X, Biris CG, et al. The origin of second harmonic generation hotspots in chiral optical metamaterials [Invited]. Opt Mater Express. 2011;1(1):36–45.

[50] Toroghi S, Kik PG. Cascaded plasmon resonant field enhancement in nanoparticle dimers in the point dipole limit. Appl Phys Lett. 2012;100(18):183105.

[51] Wang FX, Rodríguez FJ, Albers WM, et al. Surface and bulk contributions to the second-order nonlinear optical response of a gold film. Phys Rev B. 2009;80 (23):233402.

[52] Zheng W, Liu X, Hanbicki AT, et al. Nonlinear magneto-plasmonics. Opt Mater Express. 2015;5(11):2597–2607.

[53] Dadap JI, Shan J, Eisenthal KB, et al. Second-harmonic Rayleigh scattering from a sphere of centrosymmetric material. Phys Rev Lett. 1999;83(20):4045.

Appendices. Symmetry and plasmonic effect on nonlinear optics

Appendix 1. Nonlinear susceptibility elements $\chi_{ijk}^{(2)}$ permitted by symmetry of the medium

We shall describe $\chi^{(2)}$ elements related to the symmetry of the medium based on the book written by Boyd [2], case by case.

(i) $\chi_{ijk}^{(2)}$ elements under C_{2v} symmetry

If we describe the symmetry of the metal groove surface using group theory, $C_{nv} = C_{2v}$ ($n = 2$). When some plane is rotated by $360/2 = \pi$ for the symmetry axis C, it is back in the original position.

Here, we perform the following operation to withdraw effective nonlinear susceptibilities under C_{2v} symmetry. The nonlinear polarization P^{NL} excited by the electric field E of the incident light is expressed as:

$$P^{NL}(2\omega) = \varepsilon_0 \sum_{j,k} \chi_{ijk}^{(2)} E_j E_k \ (\varepsilon_0 \approx 1) \tag{A.1}$$

First, we convert third-rank tensors of ijk to coordinate the axis of xyz. When we do not consider the symmetry, P^{NL} with x, y, and z components are given as the following equations:

$$P_x^{NL}(2\omega) = \chi_{xxx}^{(2)} E_x E_x + \chi_{xyy}^{(2)} E_y E_y + \chi_{xzz}^{(2)} E_z E_z + \chi_{xxy}^{(2)} E_x E_y \\ + \chi_{xyx}^{(2)} E_y E_x + \chi_{xxz}^{(2)} E_x E_z + \chi_{xzx}^{(2)} E_z E_x + \chi_{xyz}^{(2)} E_y E_z + \chi_{xzy}^{(2)} E_z E_y \tag{A.2}$$

$$P_y^{NL}(2\omega) = \chi_{yxx}^{(2)} E_x E_x + \chi_{yyy}^{(2)} E_y E_y + \chi_{yzz}^{(2)} E_z E_z + \chi_{yxy}^{(2)} E_x E_y \\ + \chi_{yyx}^{(2)} E_y E_x + \chi_{yxz}^{(2)} E_x E_z + \chi_{yzx}^{(2)} E_z E_x + \chi_{yyz}^{(2)} E_y E_z + \chi_{yzy}^{(2)} E_z E_y \tag{A.3}$$

$$P_z^{NL}(2\omega) = \chi_{zxx}^{(2)} E_x E_x + \chi_{zyy}^{(2)} E_y E_y + \chi_{zzz}^{(2)} E_z E_z + \chi_{zxy}^{(2)} E_x E_y \\ + \chi_{zyx}^{(2)} E_y E_x + \chi_{zxz}^{(2)} E_x E_z + \chi_{zzx}^{(2)} E_z E_x + \chi_{zyz}^{(2)} E_y E_z + \chi_{zzy}^{(2)} E_z E_y \tag{A.4}$$

The groove structure has two mirrors normal to the surface and the symmetry is broken in the z-direction. Taking this into account, the inversion operation for C_{2v} symmetry can be performed twice with respect to x- and y-axes. If we perform the inversion operation for the x-axis as ($P_x^{(2)}$, $P_y^{(2)}$, $P_z^{(2)}$)$\Rightarrow$($- P_x^{(2)}$, $P_y^{(2)}$, $P_z^{(2)}$) and (E_x, E_y, E_z)$\Rightarrow$($- E_x$, E_y, E_z) for Equations (A.2), (A.3), and (A.4), they are modified as Equations (A.5), (A.6), and (A.7):

$$-P_x^{NL}(2\omega) = \chi_{xxx}^{(2)} E_x E_x + \chi_{xyy}^{(2)} E_y E_y + \chi_{xzz}^{(2)} E_z E_z - \chi_{xxy}^{(2)} E_x E_y \\ - \chi_{xyx}^{(2)} E_y E_x - \chi_{xxz}^{(2)} E_x E_z - \chi_{xzx}^{(2)} E_z E_x + \chi_{xyz}^{(2)} E_y E_z + \chi_{xzy}^{(2)} E_z E_y \tag{A.5}$$

$$P_y^{NL}(2\omega) = \chi_{yxx}^{(2)} E_x E_x + \chi_{yyy}^{(2)} E_y E_y + \chi_{yzz}^{(2)} E_z E_z - \chi_{yxy}^{(2)} E_x E_y \\ - \chi_{yyx}^{(2)} E_y E_x - \chi_{yxz}^{(2)} E_x E_z - \chi_{yzx}^{(2)} E_z E_x + \chi_{yyz}^{(2)} E_y E_z + \chi_{yzy}^{(2)} E_z E_y \tag{A.6}$$

$$P_z^{NL}(2\omega) = \chi_{zxx}^{(2)} E_x E_x + \chi_{zyy}^{(2)} E_y E_y + \chi_{zzz}^{(2)} E_z E_z - \chi_{zxy}^{(2)} E_x E_y \\ - \chi_{zyx}^{(2)} E_y E_x - \chi_{zxz}^{(2)} E_x E_z - \chi_{zzx}^{(2)} E_z E_x + \chi_{zyz}^{(2)} E_y E_z + \chi_{zzy}^{(2)} E_z E_y \tag{A.7}$$

When Equations (A.5), (A.6), and (A.7) given by the inversion operation have the same sign as Equations (A.2), (A.3), and (A.4) given by the identity operation, the same terms remain, as shown below:

$$P_x^{NL}(2\omega) = \chi_{xxy}^{(2)} E_x E_y + \chi_{xyx}^{(2)} E_y E_x + \chi_{xxz}^{(2)} E_x E_z + \chi_{xzx}^{(2)} E_z E_x \tag{A.8}$$

$$P_y^{NL}(2\omega) = \chi_{yxx}^{(2)} E_x E_x + \chi_{yyy}^{(2)} E_y E_y + \chi_{yzz}^{(2)} E_z E_z + \chi_{yyz}^{(2)} E_y E_z \\ + \chi_{yzy}^{(2)} E_z E_y \tag{A.9}$$

$$P_z^{NL}(2\omega) = \chi_{zxx}^{(2)} E_x E_x + \chi_{zyy}^{(2)} E_y E_y + \chi_{zzz}^{(2)} E_z E_z + \chi_{zyz}^{(2)} E_y E_z \\ + \chi_{zzy}^{(2)} E_z E_y \tag{A.10}$$

If we next perform the inversion operation for the y-axis as ($P_x^{(2)}$, $P_y^{(2)}$, $P_z^{(2)}$)$\Rightarrow$($P_x^{(2)}$, $- P_y^{(2)}$, $P_z^{(2)}$) and (E_x, E_y, E_z)$\Rightarrow$(E_x, $- E_y$, E_z) for Equations (A.8), (A.9), and (A.10), they are modified as Equations (A.11), (A.12), and (A.13):

$$P_x^{NL}(2\omega) = -\chi_{xxy}^{(2)} E_x E_y - \chi_{xyx}^{(2)} E_y E_x + \chi_{xxz}^{(2)} E_x E_z \\ + \chi_{xzx}^{(2)} E_z E_x \tag{A.11}$$

$$- P_y^{NL}(2\omega) = \chi_{yxx}^{(2)} E_x E_x + \chi_{yyy}^{(2)} E_y E_y + \chi_{yzz}^{(2)} E_z E_z \\ - \chi_{yyz}^{(2)} E_y E_z - \chi_{yzy}^{(2)} E_z E_y \tag{A.12}$$

$$P_z^{NL}(2\omega) = \chi_{zxx}^{(2)} E_x E_x + \chi_{zyy}^{(2)} E_y E_y + \chi_{zzz}^{(2)} E_z E_z - \chi_{zyz}^{(2)} E_y E_z \\ - \chi_{zzy}^{(2)} E_z E_y \tag{A.13}$$

When Equations (A.11), (A.12), and (A.13) given by the inversion operation have the same sign as Equations (A.2), (A.3), and (A.4) given by the identity operation, the same terms remain as below:

$$P_x^{NL}(2\omega) = \chi_{xxz}^{(2)} E_x E_z + \chi_{xzx}^{(2)} E_z E_x \tag{A.14}$$

$$P_y^{NL}(2\omega) = \chi_{yyz}^{(2)} E_y E_z + \chi_{yzy}^{(2)} E_z E_y \tag{A.15}$$

$$P_z^{NL}(2\omega) = \chi_{zxx}^{(2)} E_x E_x + \chi_{zyy}^{(2)} E_y E_y + \chi_{zzz}^{(2)} E_z E_z \tag{A.16}$$

If we consider the permutation ($jk \Leftrightarrow kj$) of Kleinman's symmetry, non-zero independent nonlinear susceptibility elements $\chi_{xxz}^{(2)} = \chi_{xzx}^{(2)}$, $\chi_{yyz}^{(2)} = \chi_{yzy}^{(2)}$, $\chi_{zxx}^{(2)}$, $\chi_{zyy}^{(2)}$, $\chi_{zzz}^{(2)}$ are permitted under C_{2v} symmetry with the groove surface.

(ii) $\chi_{ijk}^{(2)}$ elements under C_{4v} symmetry

If we describe the symmetry of a metal cube's (tetragonal) surface using group theory, $C_{nv} = C_{4v}$ ($n = 4$). The cube structure has four mirrors normal to the surface and the symmetry is broken in the z-direction. Taking it into account, the inversion operation for C_{4v} symmetry can be performed twice with respect to x- and y-axes and, furthermore, the permutation operation between x and y as ($P_x^{(2)}$, $P_y^{(2)}$, $P_z^{(2)}$)$\Rightarrow$($- P_y^{(2)}$, $P_x^{(2)}$, $P_z^{(2)}$), (E_x, E_y, E_z)$\Rightarrow$($- E_y$, E_x, E_z).

Under C_{2v} symmetry, five non-zero independent nonlinear susceptibility elements, $\chi_{xxz}^{(2)} = \chi_{xzx}^{(2)}$, $\chi_{yyz}^{(2)} = \chi_{yzy}^{(2)}$, $\chi_{zxx}^{(2)}$, $\chi_{zyy}^{(2)}$, $\chi_{zzz}^{(2)}$, are permitted. Here, if the permutation operation between x and y is added, three independent nonlinear susceptibility elements, $\chi_{zzz}^{(2)}$, $\chi_{zxx}^{(2)} = \chi_{zyy}^{(2)}$, $\chi_{xzx}^{(2)} = \chi_{yzy}^{(2)} = \chi_{xxz}^{(2)} = \chi_{yyz}^{(2)}$, are permitted.

Appendix 2. Local field effect on nonlinear optics

Here, we perform the expansion of local field L based on the book written by Boyd [2].

Since the polarization P has both linear and nonlinear contributions,

$$\tilde{P} = \tilde{P}^L + \tilde{P}^{NL} \tag{B.1}$$

We represent the linear contribution as

$$\tilde{P}^L = N\varepsilon_0 \alpha \tilde{E}_{loc} \tag{B.2}$$

Here, the local electric field E_{loc} is written as

$$\tilde{E}_{loc} = E + \frac{1}{3\varepsilon_0}\tilde{P} \tag{B.3}$$

Therefore, the linear polarization P^L is expanded as

$$
\begin{aligned}
\tilde{P}^L &= N\varepsilon_0 a\left(\tilde{E} + \frac{1}{3\varepsilon_0}\tilde{P}\right)\\
&= N\varepsilon_0 a\left(\tilde{E} + \frac{1}{3\varepsilon_0}\tilde{P}^L + \frac{1}{3\varepsilon_0}\tilde{P}^{NL}\right)\\
&= Na\left(\varepsilon_0\tilde{E} + \frac{1}{3}\tilde{P}^L + \frac{1}{3}\tilde{P}^{NL}\right)
\end{aligned}
\tag{B.4}
$$

Here, let us derive the linear susceptibility $\chi^{(1)}$. Generally, $\chi^{(1)}$ is defined as

$$\tilde{P}^L = \varepsilon_0\chi^{(1)}\tilde{E} \tag{B.5}$$

If we derive $\chi^{(1)}$ using Equation (B.4),

$$
\begin{aligned}
\varepsilon_0\chi^{(1)}\tilde{E} &= N\varepsilon_0 a\left(\tilde{E} + \frac{1}{3\varepsilon_0}\left(\varepsilon_0\chi^{(1)}\tilde{E}\right)\right)\\
\chi^{(1)} &= Na\left(1 + \frac{1}{3}\chi^{(1)}\right)\\
\chi^{(1)} &= \frac{Na}{\left(1 - \frac{1}{3}Na\right)}
\end{aligned}
\tag{B.6}
$$

Here, the linear dielectric constant $\varepsilon^{(1)}$ is defined as

$$\varepsilon^{(1)} = 1 + \chi^{(1)} \tag{B.7}$$

If we use Equations (6) and (7), P^L is solved as

$$
\begin{aligned}
\tilde{P}^L &= \frac{Na}{(1-\frac{1}{3})Na}\left(\varepsilon_0\tilde{E} + \frac{1}{3}\tilde{P}^{NL}\right)\\
&= \chi^{(1)}\left(\varepsilon_0\tilde{E} + \frac{1}{3}\tilde{P}^{NL}\right)\\
' &= \left[\varepsilon^{(1)} - 1\right]\left(\varepsilon_0\tilde{E} + \frac{1}{3}\tilde{P}^{NL}\right)
\end{aligned}
\tag{B.8}
$$

We next consider the displacement vector $\tilde{D}$. If the expression for P^L is substituted into $\tilde{D}$, which is derived as

$$
\begin{aligned}
\tilde{D} &= \varepsilon_0\tilde{E} + \tilde{P}\\
&= \varepsilon_0\tilde{E} + \tilde{P}^L + \tilde{P}^{NL}\\
&= \varepsilon_0\tilde{E} + \left[\varepsilon^{(1)} - 1\right]\left(\varepsilon_0\tilde{E} + \frac{1}{3}\tilde{P}^{NL}\right) + \tilde{P}^{NL}\\
&= \varepsilon^{(1)}\varepsilon_0\tilde{E} + \left(\frac{\varepsilon^{(1)} + 2}{3}\right)\tilde{P}^{NL}
\end{aligned}
\tag{B.9}
$$

Since the nonlinear source term P^{NLS} is actually the nonlinear polarization P^{NL} multiplied by the factor $(\varepsilon^{(1)}+2)/3$, $\tilde{D}$ is simply rewritten as

$$\tilde{D} = \varepsilon^{(1)}\varepsilon_0\tilde{E} + \tilde{P}^{NLS} \tag{B.10}$$

Here, we consider the wave equation. In general, the optical wave equation is written as

$$\nabla \times \nabla \times \tilde{E} + \mu_0\frac{\partial^2}{\partial t^2}\tilde{D} = 0 \tag{B.11}$$

We now use Equation (B.10) to eliminate $\tilde{D}$ from this equation. If we replace the magnetic permeability μ_0 by $1/\varepsilon_0 c^2$, we obtain the wave equation:

$$
\begin{aligned}
\nabla \times \nabla \times \tilde{E} + \frac{1}{\varepsilon_0 c^2}\frac{\partial^2}{\partial t^2}\left(\varepsilon^{(1)}\varepsilon_0\tilde{E} + \tilde{P}^{NLS}\right) &= 0\\
\nabla \times \nabla \times \tilde{E} + \frac{\varepsilon^{(1)}}{c^2}\frac{\partial^2}{\partial t^2}\tilde{E} &= -\frac{1}{\varepsilon_0 c^2}\frac{\partial^2}{\partial t^2}\tilde{P}^{NLS}
\end{aligned}
\tag{B.12}
$$

This equation shows that the local field effects are incorporated into the wave equation.

We finally define the relation between the second-order nonlinear polarization $P(2\omega)$ and the nonlinear susceptibility $\chi^{(2)}$. The nonlinear polarization $P(2\omega)$ in the metal structures at the SH frequency is written as a function of the incident electric field E at ω as

$$P_i(2\omega) = \varepsilon_0\chi^{(2)}_{ijk}(-2\omega : \omega, \omega) : E_j(\omega)E_k(\omega) \tag{B.13}$$

where χ_{ijk} is the third-rank tensor of nonlinear susceptibility, while i, j, and k represent any of the Cartesian coordinates X, Y, and Z. The coordinate system is oriented so that the X and Y coordinates are in the plane and the Z coordinate is in the direction normal to the substrate surface. Here, if we assume that the local electric field $E_{loc} = L(\omega)E(\omega)$, where $L(\omega)$ represents that the local field factors at the fundamental frequency, the nonlinear polarization P^{NL} can be written as follows:

$$
\begin{aligned}
P^{NL}_i(2\omega) &= \varepsilon_0 L_i(2\omega)\sum_{j,k}\chi^{(2)}_{ijk}(-2\omega : \omega, \omega)\\
&: L_j(\omega)E_j(\omega)L_k(\omega)E_k(\omega)
\end{aligned}
\tag{B.14}
$$

By solving Equation (12), P^{NLS} is given as

$$P^{NLS}(2\omega) = \varepsilon_0\sum_{j,k}\chi^{(2)}_{ijk}(-2\omega : \omega, \omega)E_j(\omega)E_k(\omega) \tag{B.15}$$

As mentioned above, the relation between P^{NLS} and P^{NL} is $P^{NLS} = (\varepsilon^{(1)} + 2)/3\; P^{NL}$. Thus, P^{NL} is given as

$$
\begin{aligned}
P^{NL}_i(2\omega) &= \left(\frac{\varepsilon^{(1)}(2\omega) + 2}{3}\right)\varepsilon_0\sum_{j,k}\chi^{(2)}_{ijk}(-2\omega\\
&: \omega, \omega)L_j(\omega)E_j(\omega)L_k(\omega)E_k(\omega)
\end{aligned}
\tag{B.16}
$$

Using Equations (B.3), (B.5), and (B.7), we relate local and macroscopic fields E_{loc} and E as

$$
\begin{aligned}
\tilde{E}_{loc} &= \tilde{E} + \frac{1}{3}\chi^{(1)}\tilde{E}\\
&= \left[1 + \frac{1}{3}\left(\varepsilon^{(1)} - 1\right)\right]\tilde{E}\\
&= \left(\frac{\varepsilon^{(1)} + 2}{3}\right)\tilde{E}
\end{aligned}
\tag{B.17}
$$

Therefore, using the relation $L(\omega) = (\varepsilon^{(1)} + 2)/3$, P^{NL} is rewritten as

$$
\begin{aligned}
P^{NL}_i(2\omega) &= \left(\frac{\varepsilon^{(1)}(2\omega) + 2}{3}\right)\varepsilon_0\sum_{j,k}\chi^{(2)}_{ijk}(-2\omega\\
&: \omega, \omega)\left(\frac{\varepsilon^{(1)}(\omega) + 2}{3}\right)^2 E_j(\omega)E_k(\omega)
\end{aligned}
\tag{B.18}
$$

This equation shows that the nonlinear polarization P^{NL} including L factors is dominated by the linear dielectric $\varepsilon^{(1)}$. Thus, we can say that SP excitation is very sensitive to the linear dielectric change, and SP excitation can lead to SHG enhancement from this equation.